Stockholm University

Bachelor Thesis

Degree Project in
Marine Geosciences, 30 hp

Sediment Deformation Beneath Sites of Glacial Erosion in the Central Arctic Ocean

Felicia Carlsson

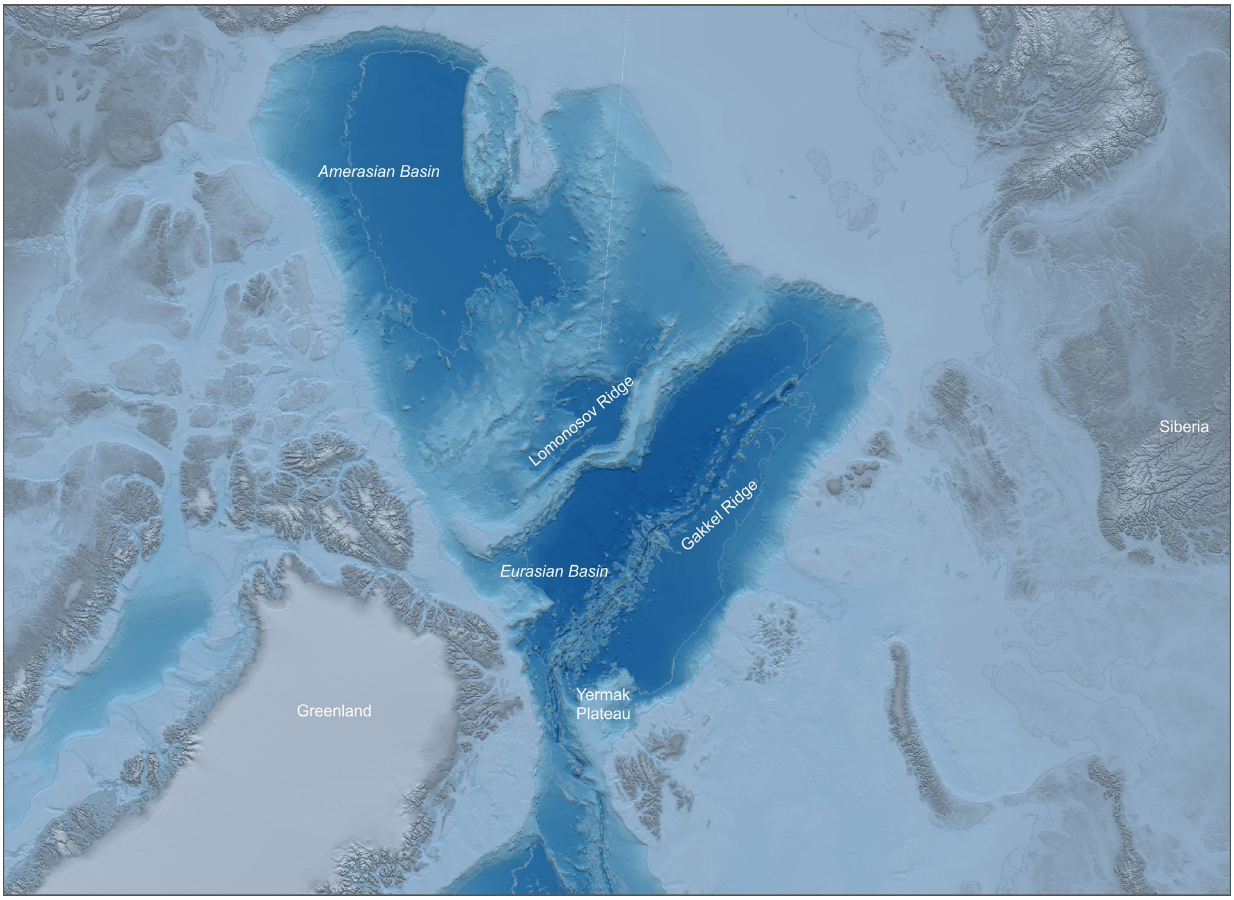

Stockholm 2026

Department of Geological Sciences
Stockholm University
SE-106 91 Stockholm

ABSTRACT

The Lomonosov Ridge is an 1800 km-long bathymetric high that extends across the central Arctic Ocean from the Greenland margin to the Siberian shelf. It is characterised by a complex geomorphology and a glacially influenced history, with evidence of large-scale glacial erosion in water depths of <1000 m. This study investigates five sediment cores collected from the ridge using a combination of geotechnical analyses, sedimentological observations and CT imaging to investigate the degree of subglacial deformation in areas of ice scour and erosion.

Previous studies have attempted to determine whether sediments beneath erosion horizons are heavily remoulded or remain intact when the overlying sediments were eroded. This study builds on this previous work and incorporates CT-scanning data, in an attempt to better resolve these processes. The aim is to investigate how subglacial deformation may have affected the sediments and their geotechnical properties and test the hypothesis that sediments with low undrained shear strength are indicative of glacial remoulding during erosion.

Inter-core correlation reveals similar stratigraphic sequences above a common erosional horizon, but highlights pronounced differences in the undrained shear strength in the underlying sediments. However, CT-scanning does not show any pronounced signs of sediment deformation. Instead, the calculated Overconsolidation Ratio (OCR) values suggest that erosion was less extensive at sites located in deeper water. This is consistent with the predicted erosion of material under glacial ice with a fixed thickness.

The results presented in this study contribute to the understanding of the geotechnical properties of sediments beneath regions of ice scouring and provide further insight into the glacial processes affecting the central segment of the Lomonosov Ridge.

Index

Introduction

The Lomonosov Ridge, approximately 1800 km in length, divides the Arctic Ocean into the Amerasian and Eurasian basins (Kristoffersen et al., 2024). It is considered a double-sided passive margin that was rifted from the Barents-Kara shelf when seafloor spreading commenced along the Gakkel Ridge in the early Cenozoic (Jokat et al., 1992). Due to variations in geomorphology and structural trend, the ridge can be described according to three different sections: The Siberian segment, the Central segment and the North American segment (Kristoffersen et al., 2024).

Comparison between the geomorphology of the Amerasian flank and the Eurasian flank reveals variations in slope, with slopes ranging from <3° to ~6° on the Amerasian Basin side. On the Eurasian basin facing side the ridge's geomorphology displays a more complex style with stair-like structures and a prominent difference in relief that may reflect differences in the form of rifting along these two flanks during its geologic evolution.

The orientation and location of the ridge create an oceanic boundary across the Arctic Ocean, affecting intermediate and deep-water circulation. Passages at each end of the ridge disconnect it from the continental margins, and measurements suggest that intermittent flow occurs across the ridge (Kristoffersen et al., 2024).

Study area map of the Lomonosov Ridge, central Arctic Ocean

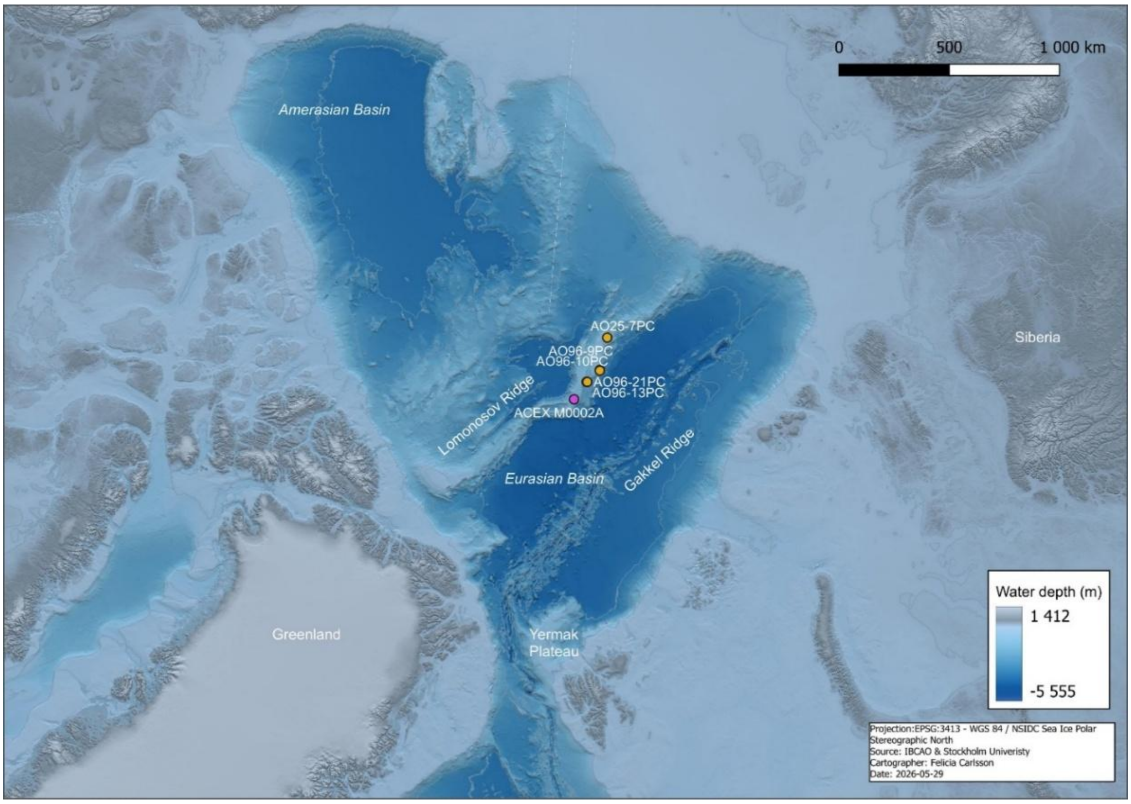

Figure 1. Bathymetric map of the central Arctic Ocean (IBCAO grid), displaying the sediment cores investigated in this study (AO96-9PC, AO96-10PC, AO96-13PC, AO96-21PC and AO25-7PC). Location of the ACEX M0002A reference core is included.

In 1996, the Arctic Ocean expedition on icebreaker *Oden* set out to investigate sediment on various locations on Lomonosov Ridge. During this expedition, high-resolution sub-bottom chirp sonar data was collected. This data displayed evidence of erosion at water depths of < 1000 m on central portions of the Lomonosov Ridge (Jakobsson, 1999).

According to Jakobsson et al. (2016) the first evidence of glacial ice grounding in intermediate to deep water locations of the Arctic Ocean was identified during seafloor surveys of the Yermak Plateau off Svalbard (Crane et al., 1997). Subsequently, extensive bathymetric, sub-bottom and coring evidence has emerged clearly illustrating glacial erosion on all mapped bathymetric highs that are shallower than 1000 meters. In the central Arctic Ocean, this has been attributed to the development of ice shelves during past glacial periods that grounded in deep water. Such ice shelves would be comparable to modern Antarctic ice shelves, which calve large tabular icebergs with draughts reaching 500–550 mbsl (Polyak et al., 2001).

During the SWERUS-C3 expedition 2014, multibeam bathymetry and sub-bottom data revealed further evidence of ice scouring and glacial landforms extending widely across the central Lomonosov Ridge (Jakobsson et al., 2016).

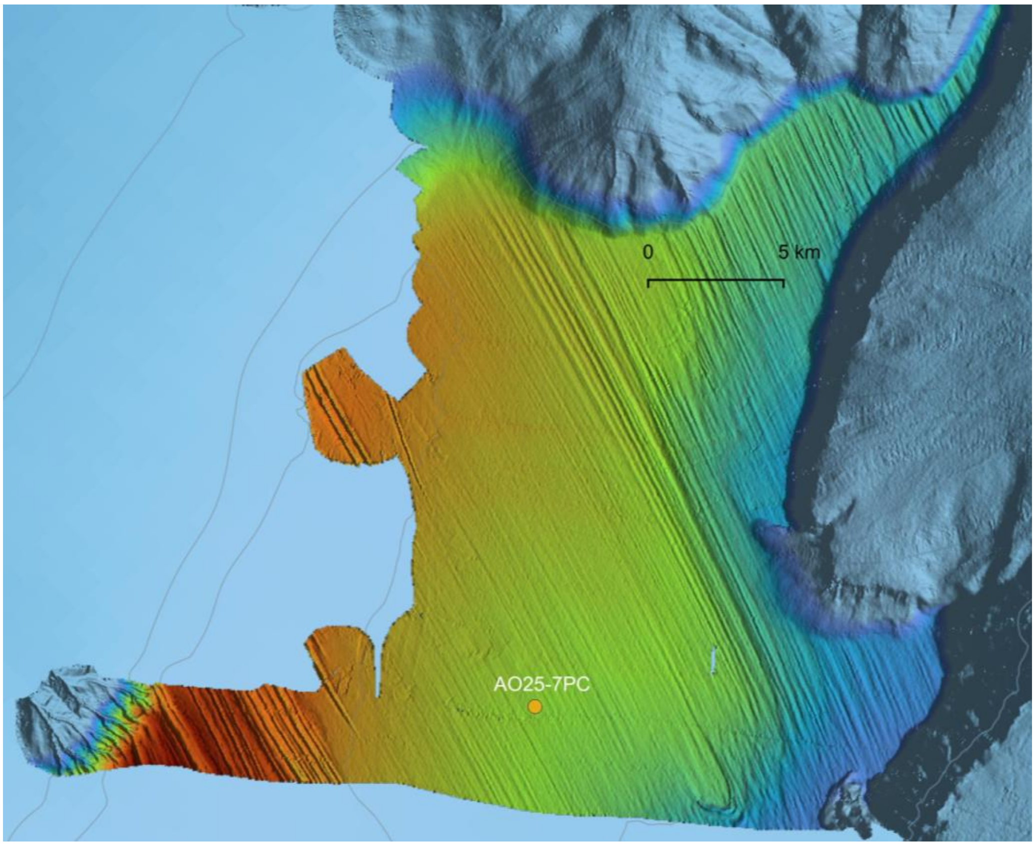

Figure 2. High-resolution bathymetric raster (50 × 50 m grid) from the central Lomonosov Ridge showing extensive, parallel glacial lineations on the ridge surface. The lineations are interpreted to reflect coherent glacial erosion and grounded ice flow rather than isolated iceberg scouring.

Unfortunately, the raw sub-bottom data from the original AO-96 expedition have been lost. However, newer data obtained from these regions during SWERUS-C3 (2014) and AO-2025 clearly show the truncation of underlying strata (AU1) by an erosional surface, overlain by an acoustically transparent interval (AU2) and capped by a conformable sediment drape (AU3) (Fig. 3).

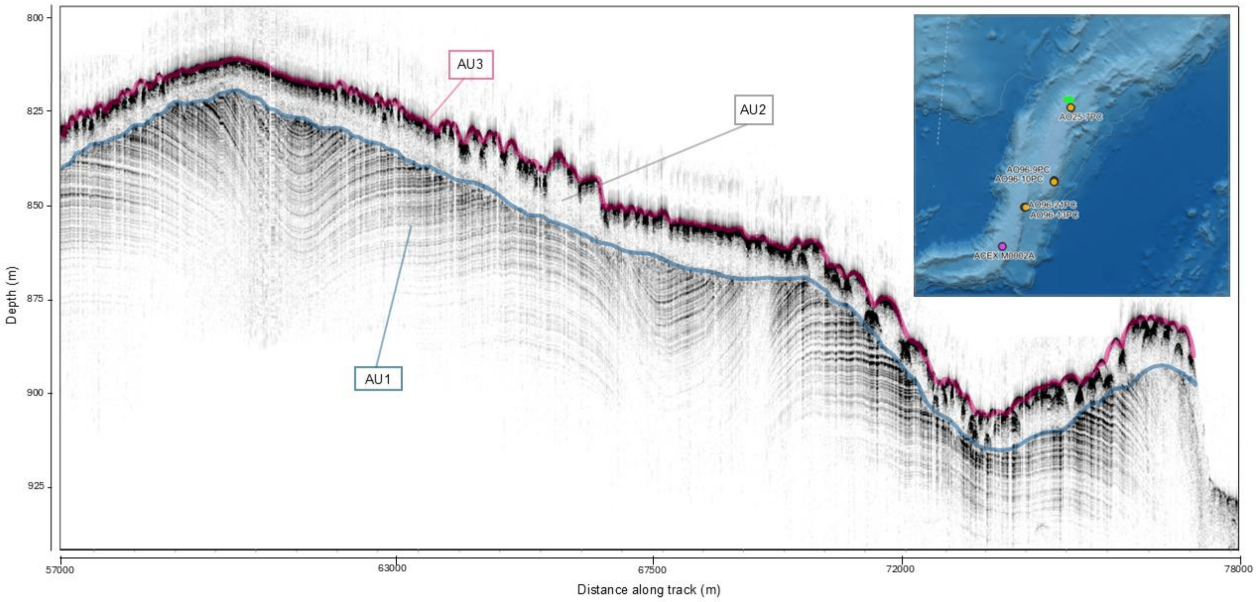

Figure 3. Sub-bottom profile collected 2025 from the central Lomonosov Ridge showing the truncation of underlying strata (AU1) by an erosional surface. The truncated strata are overlain by an acoustically transparent interval (AU2), which is capped by a conformable sediment drape (AU3). The inset map shows the location of the profile (green line) and sediment cores discussed in this study.

Studies investigating the geotechnical properties of sediments recovered from ice-scoured areas on the Lomonosov Ridge aimed to link their stress states to different glacigenic processes, including ice loading, remoulding, and erosion. The original conclusion was that sediments exhibiting low shear strength were likely representative of heavily remoulded sediments (AU2), while high shear strength sediments were interpreted as undeformed strata underlying the remoulded zone (AU1) (O'Regan et al., 2010).

Deformation in sediment cores may occur through various processes including seismicity, glaciogenic processes and coring disturbance (Cornejo et al., 2025; Stow & Aksu, 1978). Hence, when assessing a sediment's stress history, these factors need to be considered, in order to better understand the origin of observed deformation structures. Evidence of seismic deformation could, for example, include faulting, deformed lamination and folds (Cornejo et al., 2025). According to Stow and Aksu (1977), sediment deformation as a result of drilling disturbance using a piston core, may appear as inclined lamination, micro-faults, disturbed margins and even rotated blocks.

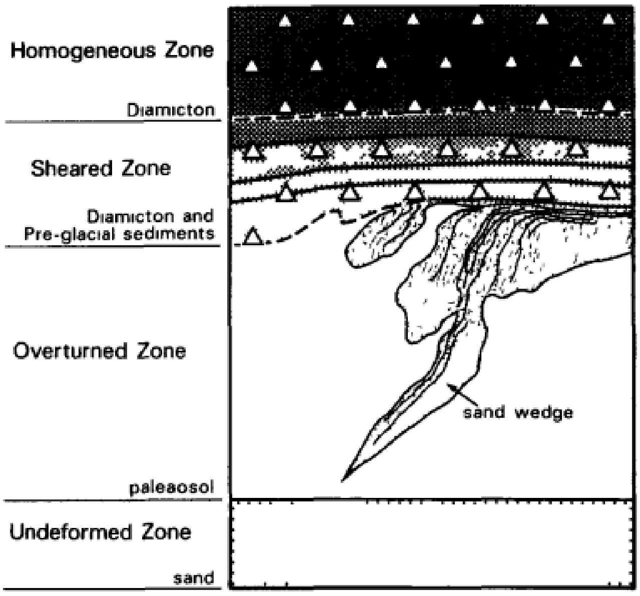

Figure 4. Illustration of subglacial deformation beneath grounded ice displaying the transition from undeformed sediments to overturned, sheared and homogenized zones. Deformation intensity increases towards the ice-bed interface (Hart and Boulton, 1991).

Subglacial deformation can occur under different conditions depending on the thermal regime of the glacier and whether the ice-bed interface is frozen or unfrozen (van der Meer, 1993). The thermal regime of the glacier bed affects the pressure melting point of the ice, and thereby whether basal melting, sliding, and sediment deformation may occur. Another important controlling factor in this process are the material properties of the bed (Clarke, G.K.C, 2005). During subglacial deformation, particles may undergo both rotational and horizontal movement (van der Meer, 1993), and structures associated with subglacial deformation may include reorientation of grains and fabric, shearing, faulting and mixing or complete remoulding (Narloch et al., 2020). Deformation is more pronounced at the ice-sediment interface and dissipates with depth below the contact horizon (Fig. 5).

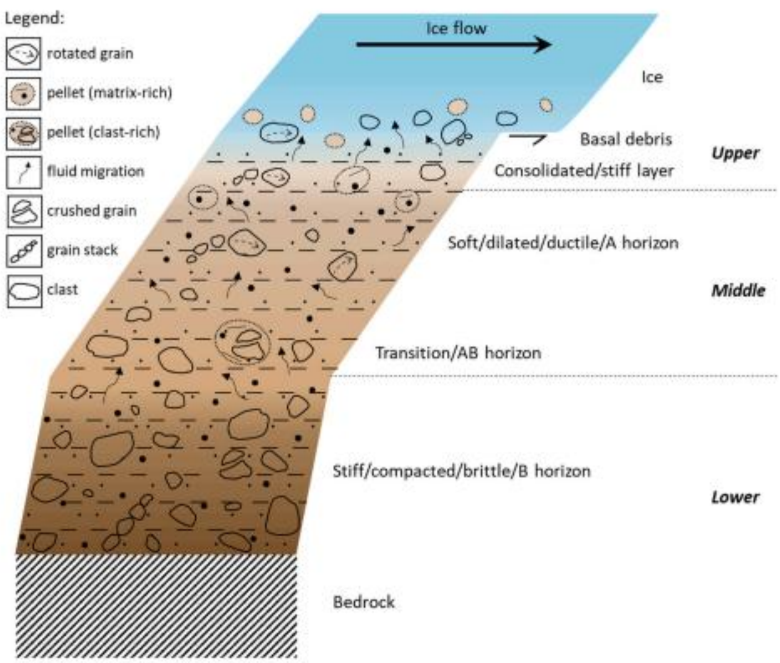

Figure 5. Conceptual model illustrating subglacial sediment deformation and associated changes in sediment structure and mechanical properties beneath flowing ice (modified from Robinson et al., 2021).

The aim of this study is to investigate how subglacial deformation has influenced the geotechnical and physical properties of Arctic Ocean sediments by analysing five sediment cores (AO96-9PC, AO96-10PC, AO96-13PC, AO96-21PC and AO25-7PC) collected from the central segment of the Lomonosov Ridge that have experienced glacial erosion (Fig. 1, Table 1). The study builds on previous work (O'Regan et al., 2010) by incorporating CT-scanning to more directly investigate the degree of remoulding and link it with the geotechnical properties of the sediments.

Methods

A combination of spatial, geotechnical, sedimentological, and imaging methods was established to conduct an analysis of sediment cores from the Lomonosov Ridge.

Core	Latitude (°N)	Longitude (°E)	Water depth (mbsl)	Core length (m)
AO96-9PC	86.414	143.444	927	2.75
AO96-10PC	86.437	143.181	947	3.14
AO96-13PC	87.153	145.169	978	4.58
AO96-21PC	87.138	144.665	987	5.67
AO25-7PC	85.148	151.380	842	4.17
ACEX (M0002A)	87.921	139.365	~1300	213.15

Table 1. Information on the sediment cores analysed in this study.

The first step was to build a bathymetric map in QGIS 3.34 using bathymetric datasets from the International Bathymetric Chart of the Arctic Ocean (IBCAO V3, 30 arc-sec grid; projection EPSG:3413). Core locations were plotted on the map, and a cross-section profile through the core positions was generated using the terrain profile tool.

CT-scanning was conducted on split cores using a GeoTek Rotating x-ray CT (RXCT) scanner in an attempt to visualise internal sediment structures and deformation features. The data were acquired at 130 kV and 500 µA, with a voxel size of 125 µm. The raw CT data were reconstructed using GeoTek Image Reconstruct. Orthogonal slices (1 mm thick) were generated using CT QuickView and exported from TIFF to JPEG format (Fig. 6).

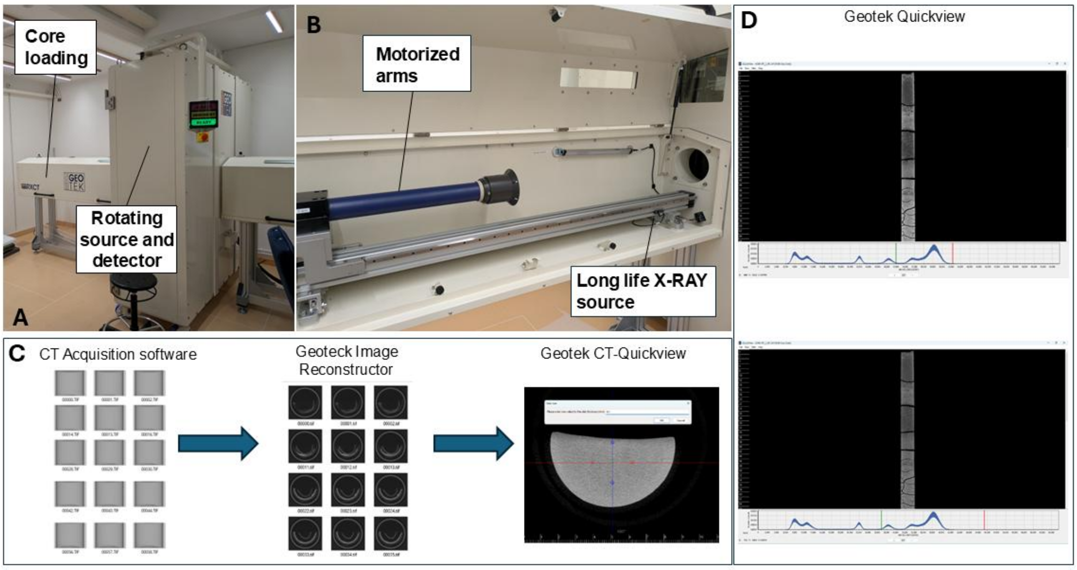

Figure 6. Workflow of the Geotek RXCT. **a)** Geotek RXCT scanner showing the rotating X-ray source and detector used during scanning. **b)** Interior view of the scanner showing the motorized core-handling system and X-ray source during core acquisition. **c)** Processing workflow from CT acquisition to image reconstruction and visualization. Each helical scan generated approximately 18.000 raw projection images, which were reconstructed into individual CT slices using Geotek Image Reconstructor. The reconstructed slices were generated at a voxel resolution of 0.1 mm and subsequently imported into Geotek CT-Quickview for visualization and analysis. d) Examples of the same CT dataset displayed using different intensity-scaling settings in Geotek CT-Quickview.

The physical and geotechnical properties (shear strength, bulk density, and magnetic susceptibility) of the sediments had been measured previously. They were plotted using Python and displayed adjacent to CT images to correlate lithostratigraphic units and identify key sedimentary structures including evidence for erosion and deformation.

Digital line-scanning images of the cores were acquired using a GeoTek Multi-Sensor core logger. In addition, the sediment cores were analysed macroscopically through visual core description, including qualitative assessment of grain size. Photo-tables for each core were created and augmented with a depth scale.

Following the compilation of geotechnical profiles, CT and digital core images, distinct zones were identified for each core. A comparative analysis was carried out between the CT images, digital core images, and the geotechnical depth profiles to investigate possible correlations between sediment structures and variations in geotechnical properties.

The next step was to carry out a comparative analysis of the subglacial sediments with lithologic units identified in the nearly 200 m Neogene succession recovered by IODP Expedition 302 (The Arctic Coring Expedition - ACEX). A photo-table of core images (sub-units 1/1–1/4) from site M0002A was created. With support from the lithostratigraphic figure presented in the expedition summary, a qualitative comparison was carried out between the lithology of Expedition 302 and the cores analysed in this study, as an attempt to assess the relative age of the sediments found beneath the ice erosional contact.

Undrained Shear strength data was used to quantitatively determine the stress history of sediments. To do this, the current in-situ effective stress was calculated using:

$\sigma v' = (\rho b - \rho w)gz$

where;

$\sigma v'$= effective vertical stress (kPa)
ρb= bulk density (kg m^{-3})
ρw= water density (1020 kg m^{-3})
g= gravitational acceleration (9.82 m s^{-2})
z= Depth erosion horizon (m)

The overconsolidation ratio (OCR) describes the stress history of the sediment, and the preconsolidation stress ($\sigma pc'$) represents the maximum past effective stress experienced by the sediment.

where OCR values indicate;

OCR >1= Overconsolidated
OCR =1= Normally consolidated
OCR <1= Underconsolidated

For each core the OCR of sediments beneath the erosional horizon was determined using the average undrained shear strength (S_u). The erosion horizon depth in each core was used as *z* in the effective stress calculation, and mean bulk density from the core top down to the erosion horizon was applied.

The OCR was estimated using the *Stress History and Normalized Soil Engineering Properties relationship* (SHANSEP) (Kassou et al., 2020) where:

$$\frac{Su}{\sigma v'} = a \cdot OCR^b$$

Where *a* and *b* are empirical SHANSEP constants relating the overconsolidation ratio to the undrained shear strength and current in-situ effective stress. These parameters are generally determined through advanced geotechnical testing, but published values are available for different soil types. For marine and normally consolidated clays, reported values commonly range between approximately 0.16–0.25 for *a* and 0.75–0.88 for *b* (Kassou et al., 2020). In this study, two sets of SHANSEP parameters were applied: *a* = 0.2 and *b* = 0.7, and *a* = 0.3 and *b* = 0.9.

The preconsolidation stress ($\sigma pc'$) was calculated from:

$$OCR = \frac{\sigma pc'}{\sigma v'}$$

Based on these calculations, the amount of eroded sediment was estimated using:

$$z_{\text{eroded}} = \frac{\Delta\sigma'}{(\rho b - \rho w) * g}$$

where;

$\Delta\sigma'$= difference between $\sigma pc'$ and $\sigma v'$
z_{eroded}= estimated thickness of eroded sediment (m)

Results

Complete core photo tables, including core photographs and corresponding CT images, are provided in Appendix A (Figures A1–A5). Several of the cores recovered during the AO96 expedition exhibit varying degrees of desiccation, which may have affected the preservation and visibility of structures associated with sediment deformation.

AO96-9PC:

AO96-9PC consists of two sections dominated by rather homogeneous brown to green-grey lithologies, interspersed with intervals of large-scale lamination in both sections. Relatively low and stable shear strength values (4.3–15 kPa) are observed down to approximately 1.7 mbsf. Below this depth, shear strength displays a near-linear increase towards the base of the core. Bulk density (BD) values remain close to 2.0 g cm^{-3} from ~0.15 to ~0.9 mbsf, after which they decrease before returning to similarly elevated values at approximately 1.7 mbsf. Magnetic susceptibility (MS) displays relatively stable values throughout the core, except for a pronounced peak in the uppermost interval.

The inferred erosion horizon was placed at approximately 1.7 mbsf (Fig. 7). This interpretation is supported by the transition from relatively low and stable shear strength values above the horizon to increasing shear strength below it, together with the return to elevated bulk density values.

The core can be divided into a post-erosion drape overlying sub-erosion sediment. Below the erosion horizon, macro-scale bends can be observed in the digital core image and corresponding CT image throughout section 2. A representative close-up from this interval is shown in Fig 7b.

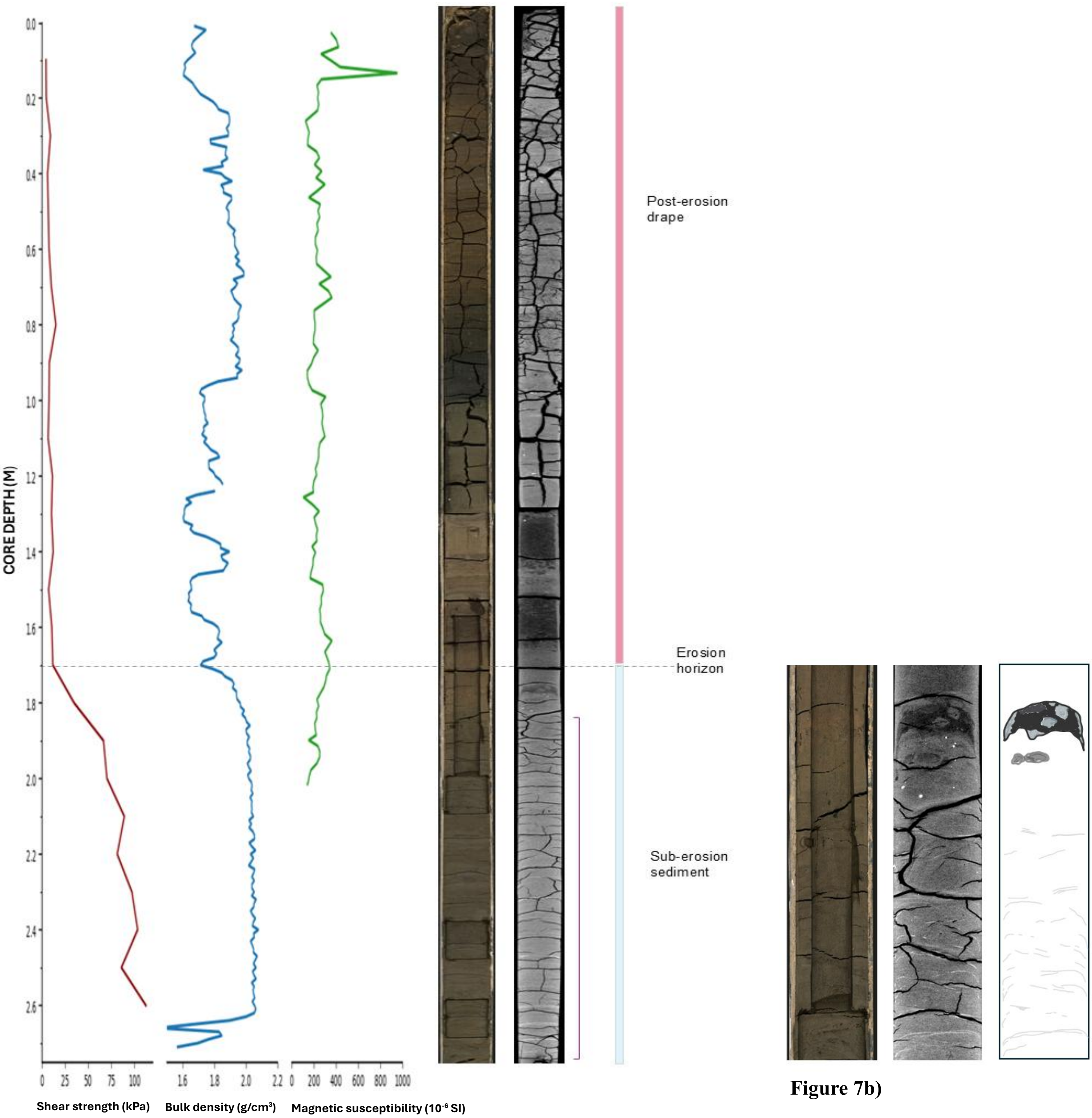

Figure 7b)

Figure 7. a) Integrated overview of AO96-9PC showing shear strength, bulk density, magnetic susceptibility, core photograph and CT image. The inferred erosion horizon separates the post-erosion drape from the underlying sub-erosion sediments. The purple bracket highlights the interval containing macro-scale curved structures below the erosion horizon. **Figure 7. b)** A representative close-up from this interval, together with the corresponding CT image and interpretation, grey lineations highlight non-planar structures visible in the CT image that may be associated with deformation.

AO96-10PC:

AO96-10PC is dominated by relatively homogeneous brown to tan lithologies with gradual shifts towards green-grey sediment throughout its three sections.

Up to ~2.4 mbsf, shear strength values are relatively low and stable (7.9–18.7 kPa), after which an increase occurs. At 2.8 mbsf, shear strength reaches its peak value of 91.9 kPa. Bulk density shows relatively stable values of approximately 2.0 g cm^{-3}, with a few dips down to around 1.6 g cm^{-3}. At approximately 2.2 mbsf, bulk density increases again. The inferred erosion horizon was placed at approximately 2.35 mbsf (Fig. 8a). This interpretation is supported by the transition from relatively low and stable shear strength values above the horizon to increasing shear strength below it, together with a more consistent pattern in bulk density. A disturbed interval is observed at approximately 2.8 mbsf. CT observations reveal horizontal and oblique structures that may reflect sediment disturbance or deformation within this interval (Fig. 8b). In the corresponding core photograph, diffuse inclined lineations on a centimetre-scale are visible within the same interval (Fig. 8c).

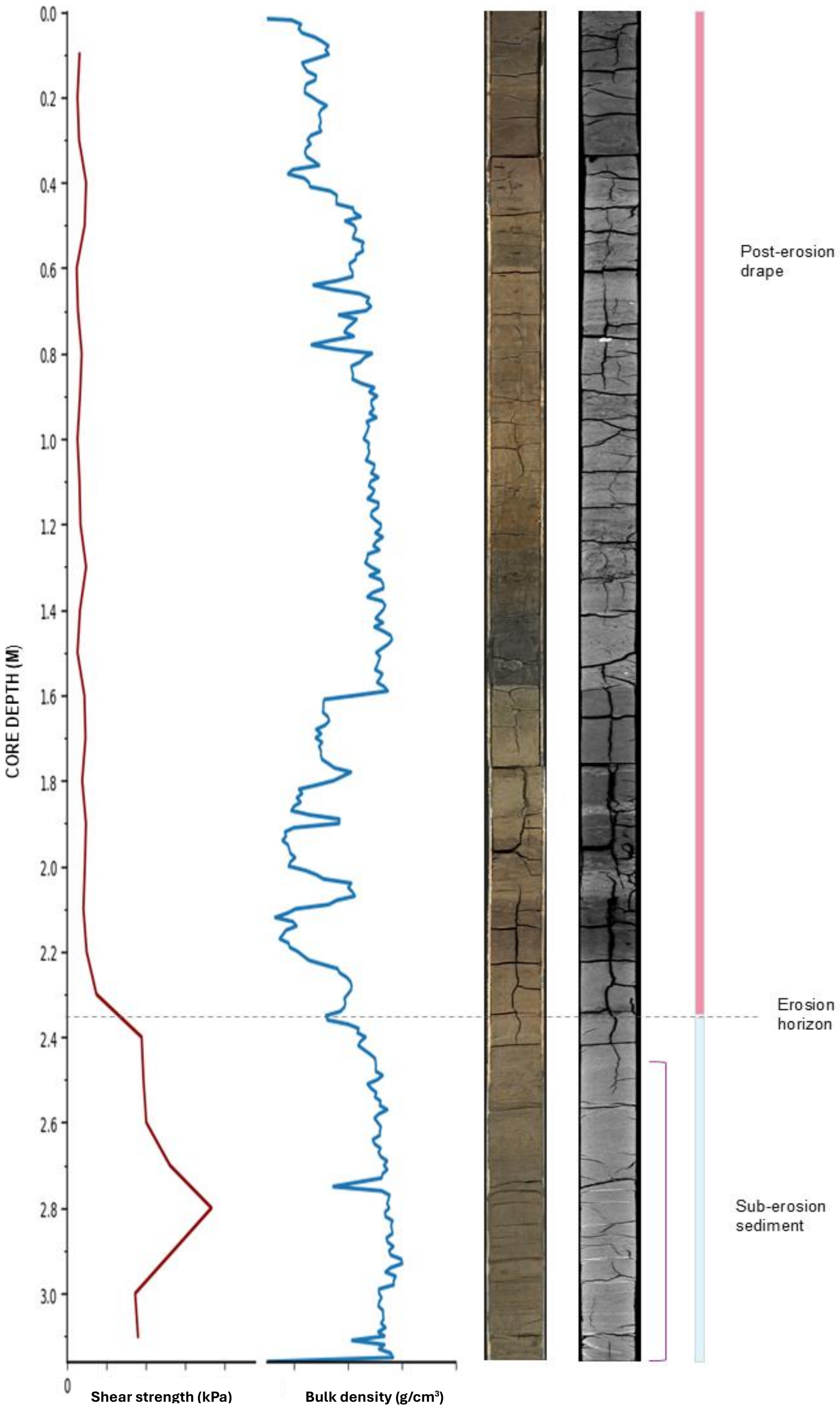

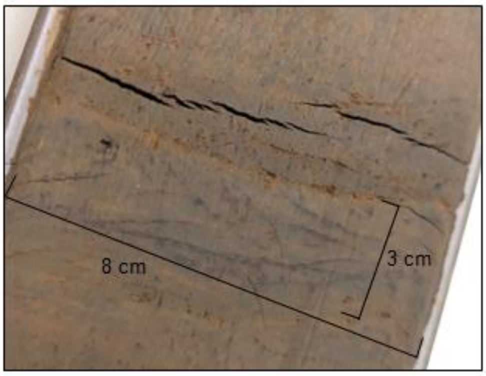

Figure 8c

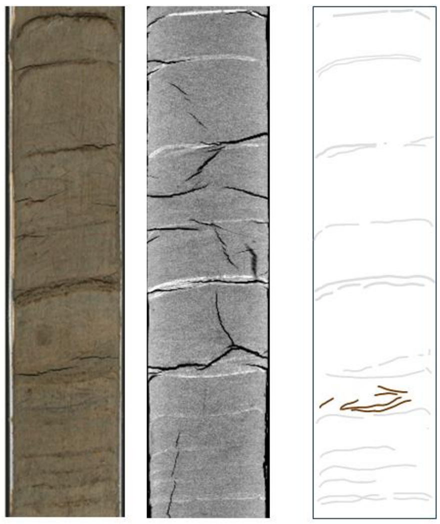

Figure 8b

Figure 8. a) Integrated overview of AO96-10PC showing shear strength, bulk density, core photograph and CT image. The inferred erosion horizon separates the post-erosion drape from the underlying sub-erosion sediments. The purple bracket highlights the disturbed interval discussed in the text. **b)** Representative close-up from the highlighted interval showing the core photograph, corresponding CT image and interpretation. Brown lineations indicate diffuse inclined structures observed in the core photograph, whereas grey lineations highlight horizontal and oblique structures visible in the CT image. **c)** Detailed core photograph showing the diffuse inclined lineations observed within the disturbed interval.

AO96-13PC:

AO96-13PC contains four sections characterised by relatively homogeneous brown to tan lithologies, gradual colour variations, and locally disturbed intervals. A porous and disturbed interval occurs within section two, while section three remains relatively homogeneous except for an abrupt lithological change at approximately 2.2 mbsf. In section four, disturbance increases downcore and the lowermost interval displays weak large-scale lamination. CT observations reveal horizontal structures within the disturbed interval selected for detailed examination that may reflect sediment disturbance or deformation (Fig. 9b).

Shear strength values vary between 1.4 and 28 kPa throughout the core, with considerable variations in magnitude in the lower interval between ~4.0 and 4.4 mbsf. Up to ~1.7 mbsf, bulk density ranges from ~1.7 to 1.9 g cm^{-3}, after which a decrease to approximately 1.7 g cm^{-3} is observed. Overall, bulk density remains relatively even throughout the core. Magnetic susceptibility varies throughout the core, with values commonly ranging between ~200 and 400×10^{-6} SI, including several lower and higher peaks. The inferred erosion horizon was placed at approximately 2.6 mbsf (Fig. 9a). Below this depth, the physical properties display a more homogenous pattern compared to the overlying sediments. Deformation-related structures are observed below the interpreted erosion horizon.

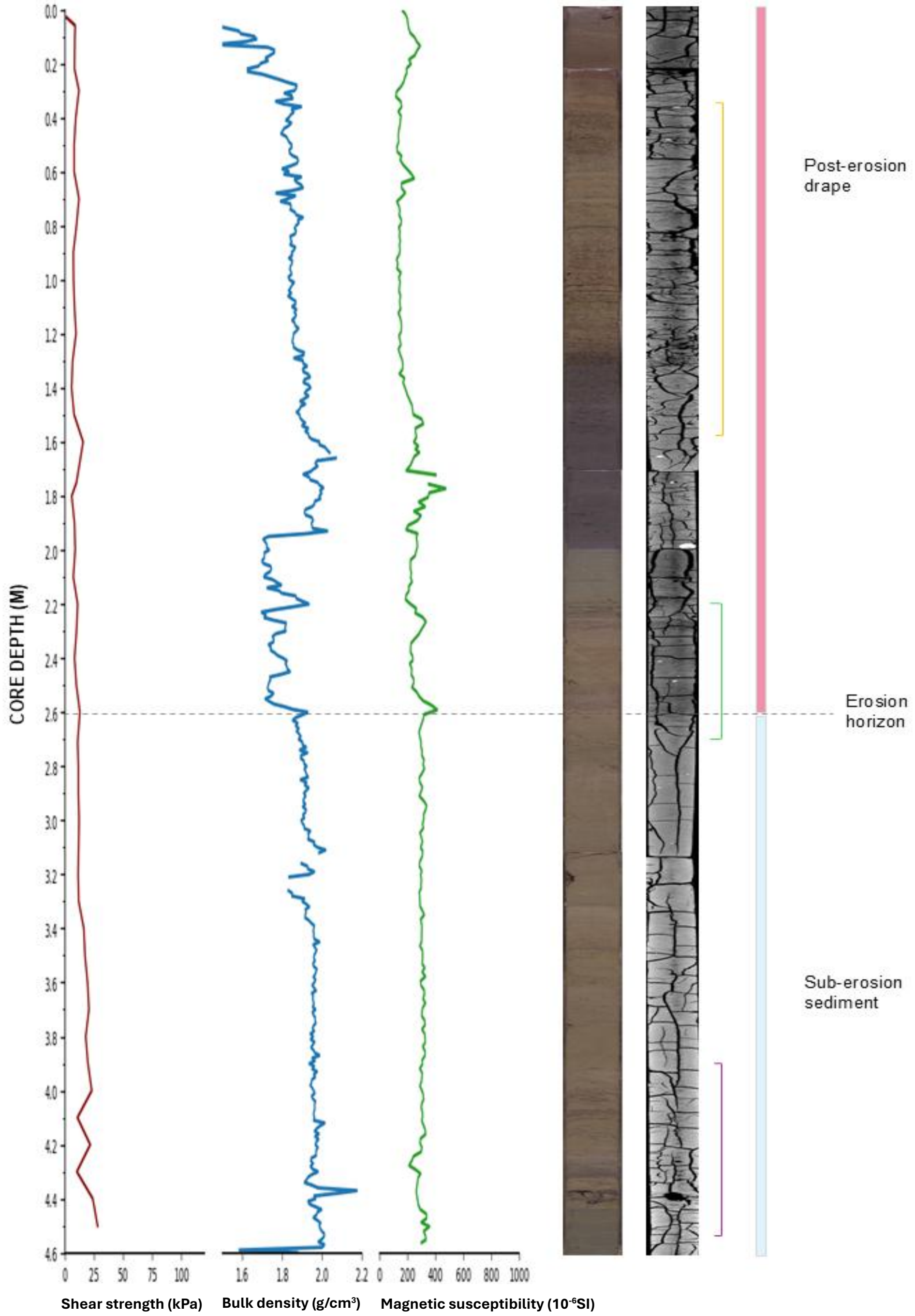

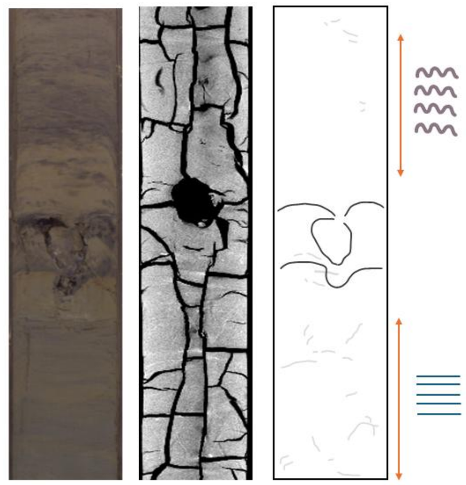

Figure 9b

Figure 9. a) Integrated overview of AO96-13PC showing shear strength, bulk density, magnetic susceptibility, core photograph and CT image. The inferred erosion horizon separates the post-erosion drape from the underlying sub-erosion sediments. The yellow bracket highlights a porous and disturbed interval, the green bracket marks an abrupt lithological change, and the purple bracket indicates the disturbed interval selected for detailed examination. **b)** Representative close-up from the interval highlighted by the purple bracket showing the core photograph, corresponding CT image and interpretation. Grey lineations indicate structures visible in the CT image. The interpretation also highlights weak large-scale lamination (blue symbols) and disturbed interval (lilac waves).

AO96-21PC:

AO96-21PC is characterised by four sections with lithologies dominated by different shades of brown, green-grey, and light-brown sediment. Intervals of smeared laminations, disturbance, and bioturbation occur throughout the core. Section 2 contains a disturbed dark-brown interval in its upper part and an abrupt lithological change at approximately 2.46 mbsf. Section 3 is generally light-brown with a locally patchy interval, while section 4 is characterised by increasingly disturbed and smeared lithologies. CT observations reveal locally inclined structures within the disturbed intervals (Fig. 10b), but few other possible signs of deformation.

Undrained shear strength ranges from 5.5 to 26.3 kPa throughout the core, with a general increase from approximately 2.7 mbsf. Bulk density is relatively stable (~1.8–2.01 g cm^{-3}) down to approximately 2.0 mbsf, where it decreases to ~1.75 g cm^{-3}. These relatively stable values of ~1.8–1.9 g cm^{-3} are reached again at approximately 3.1 mbsf.

The inferred erosion horizon was placed at approximately 2.9 mbsf (Fig. 10a). This interpretation is based on the transition towards a more homogenous pattern in the physical properties below the horizon, particularly the return to more consistent bulk density values. The occurrence of disturbed and inclined lithologies within the underlying sediments, visible in both the core photograph and corresponding CT image, was considered as part of the erosion-horizon interpretation.

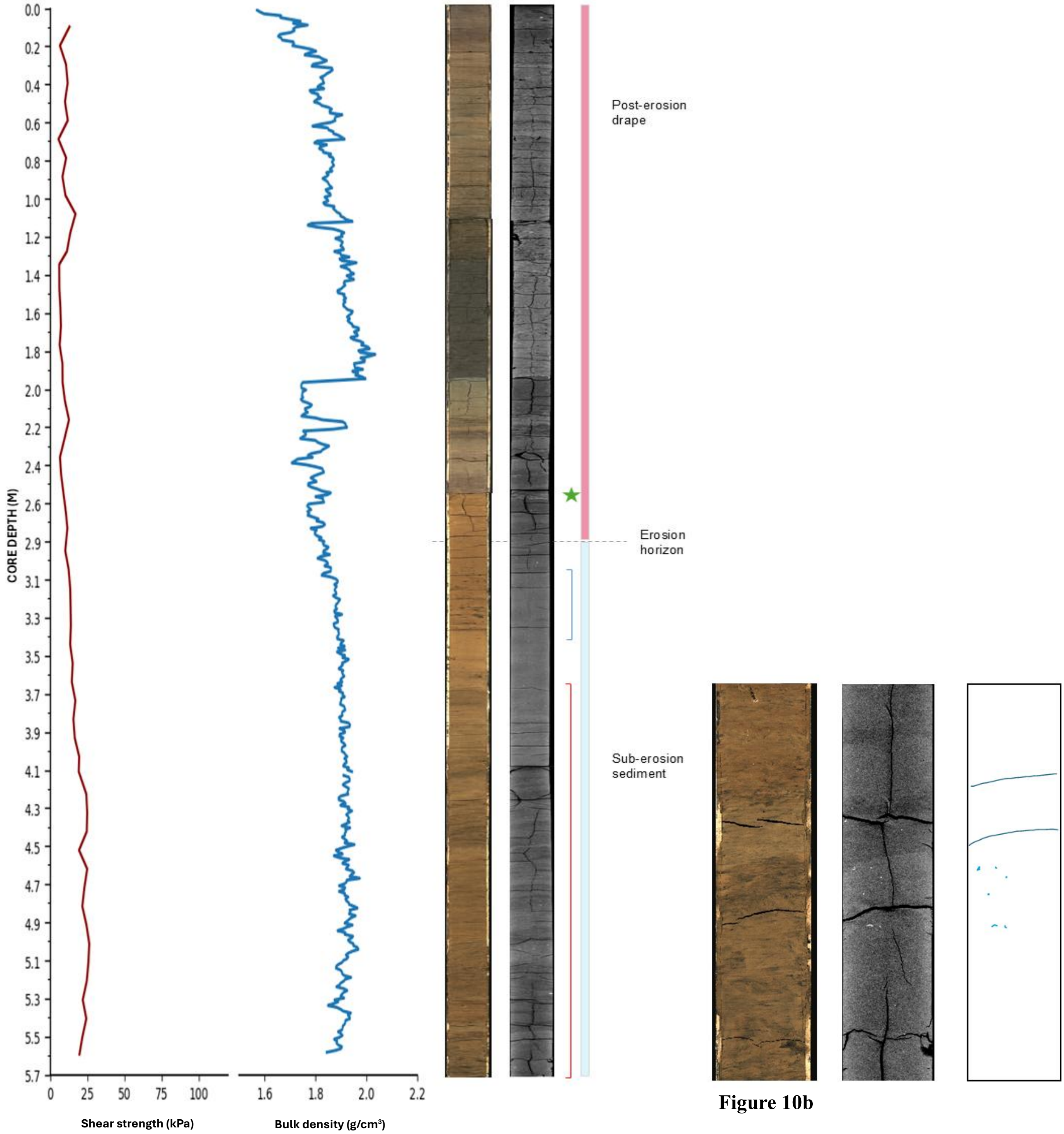

Figure 10. a) Integrated overview of AO96-21PC showing undrained shear strength, bulk density, core photograph and CT image. The inferred erosion horizon separates the post-erosion drape from the underlying sub-erosion sediments. The green star marks an abrupt lithological change, the blue bracket highlights a patchy interval, and the red bracket indicates the disturbed interval selected for detailed examination. **b)** Representative close-up from the disturbed interval showing the core photograph, corresponding CT image and interpretation. Blue lineations indicate inclined lithological boundaries that can be traced in both the core photograph and CT image.

AO25-7PC:

AO25-7PC is composed of three sections with colour variations between brown, beige, and green-grey lithologies. Variations in the level of disturbance, ranging from moderate to more pronounced, are visible throughout the core and increase downcore. In the lowermost interval, CT observations reveal several small-scale inclined and randomly oriented lineations. These diffuse lineations coincide with a centimetre-scale possible deformation structure, this interval was selected for close-up observation (Fig. 11b).

This core has a peak shear strength of 91.04 kPa, with a steady increase from approximately 3.45 mbsf. Bulk density varies until around 2.7 mbsf, below which more stable values are observed, ranging between ~1.78 and 1.98 g cm^{-3}. Magnetic susceptibility values mostly vary between 180 and 260 $\times10^{-6}$ SI, with peaks up to ~357 $\times10^{-6}$ SI.

The inferred erosion horizon was placed at approximately 2.69 mbsf (Fig. 11a). This interpretation is based on the transition towards more stable bulk density values below the horizon, together with the gradual increase in shear strength observed within the underlying sediments. The occurrence of possible deformation structures and diffuse inclined lineations below the interpreted horizon was also considered as part of the erosion-horizon interpretation.

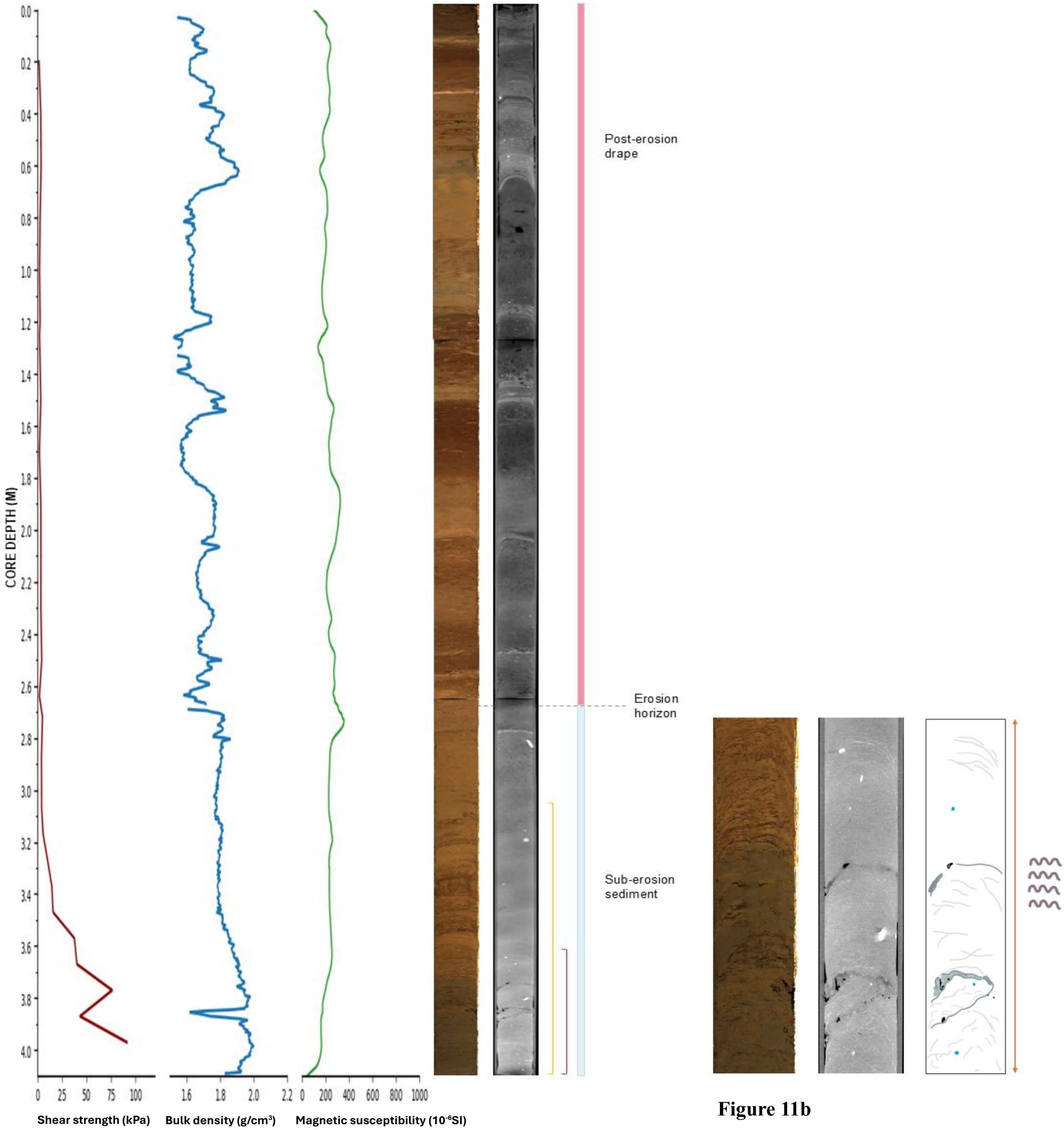

Figure 11b

Figure 11. a) Integrated overview of AO25-7PC showing shear strength, bulk density, magnetic susceptibility, core photograph and CT image. The inferred erosion horizon separates the post-erosion drape from the underlying sub-erosion sediments. The yellow bracket highlights an interval characterised by increasing disturbance, while the purple bracket marks the interval selected for detailed examination. **b)** Representative close-up from the highlighted interval showing the core photograph, corresponding CT image and interpretation. Grey lineations indicate structures visible in the CT image, while the interpretation highlights diffuse inclined lineations and a possible deformation structure identified within the interval.

Stratigraphic correlation

All the sites exhibit the same stratigraphic sequence above the inferred erosional horizon (Fig. 12). This is important as it indicates that the age of glacial erosion was the same at all locations. All cores contain a notable high density upper unit with a sharp basal contact interpreted as a diamict layer. This interval begins between approximately 0.18 and 0.40 mbsf and extends downcore to depths ranging from 0.72 and 2.0 mbsf. Within this layer, bulk density commonly ranges between ~1.84 and 1.95 g cm^{-3} in the AO96 cores, whereas AO25-7PC displays lower values of approximately ~1.70–1.85 g cm^{-3}.

AO96-9PC and AO96-10PC display relatively similar sediment characteristics within this interval, dominated by a rather homogeneous lithology, although local laminations occur in AO96-9PC. In contrast, AO96-13PC, AO96-21PC and AO25-7PC display a more variable lithology with visually interpreted disturbed intervals.

This upper unit is followed by a decrease in bulk density in all cores, which is subsequently followed by a high-density interval (purple band) (Fig. 12). In the AO96 cores, bulk-density within this depth range vary between approximately 1.80 and 1.93 g cm^{-3}. The corresponding depth interval in AO25-7PC displays lower values (~1.74–1.83 g cm^{-3}), but remains locally elevated relative to the surrounding sediment. Beneath this interval, the bulk-density records display a characteristic pattern of alternating higher and lower values, suggesting alternations between relatively finer- and coarser-grained sediments.

A further correlation can be observed near the interpreted erosion horizons. At this level, a second high-density interval (orange band) appears (Fig. 12). Sediments within this interval are relatively homogeneous in AO96-9PC and AO96-10PC, with only minor local disturbance in the latter core. In contrast, AO96-13PC, AO96-21PC and AO25-7PC display a greater degree of lithological variability and disturbance.

Beneath the erosion horizons, within the terminating interval of the cores, bulk density generally remains relatively steady. Core photographs and corresponding CT images indicate that lithological disturbance below the erosion horizon is most pronounced in AO96-13PC, AO96-21PC and AO25-7PC (Figs. 9–11).

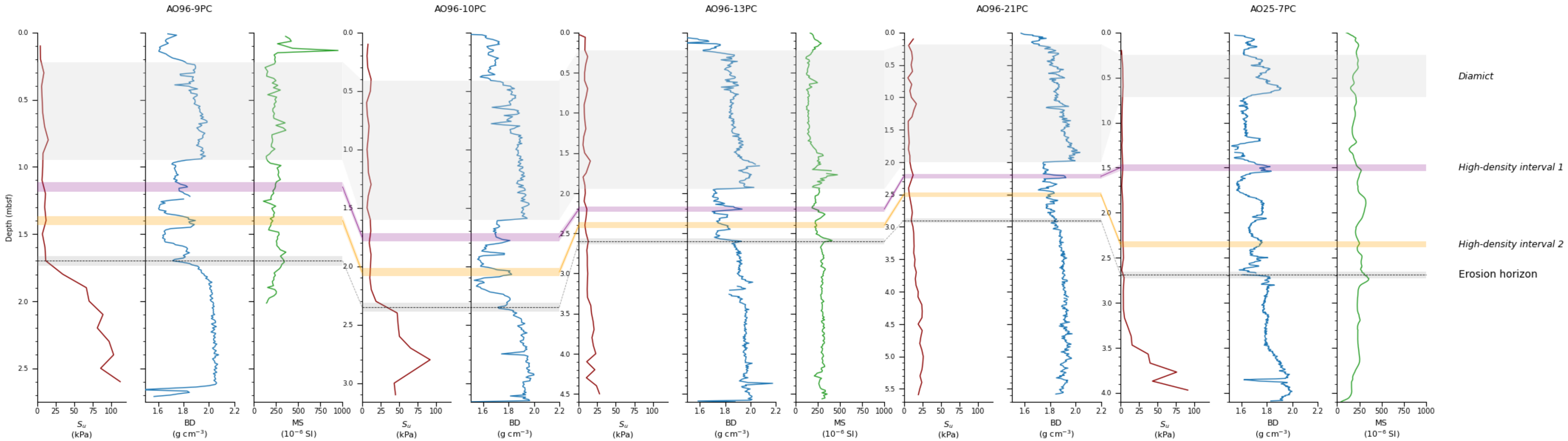

Figure 12. Stratigraphic correlation between the studied sediment cores. Dashed grey lines indicate interpreted erosion horizons, purple and orange bands indicate correlated high-density intervals, and grey shading marks the diamict interval.

Comparison ACEX stratigraphy

The nearly 200 m of Neogene sediments recovered during the Arctic Coring Expedition in 2004 were used as a reference to compare the lithologies of sediments underlying the erosion horizon. ACEX was drilled in an area that was not impacted by glacial erosion. According to the lithostratigraphic description of Expedition 302 Scientists (2006), subunit 1/1 is described as a silty clay and silty mud unit displaying brown, yellow-brown, olive-brown, red-brown and grey colours. Subunit 1/2 is described as a silty clay unit characterised by light olive-brown colours together with darker brown intervals and very dark grey mottling. Subunit 1/3 is described as a silty clay and silty mud unit displaying pronounced variations of olive, olive-grey and olive-brown colours together with darker grey intervals. Lastly, subunit 1/4 is described as a silty clay unit consisting of dark-brown, brown and dark-grey colours together with pale-brown intervals.

A qualitative comparison with AO96-9PC, AO96-10PC, AO96-13PC, AO96-21PC and AO25-7PC indicates that the lithologies observed beneath the erosion horizons show the strongest similarities to subunit 1/3, particularly with respect to the olive, olive-grey and olive-brown colour variations. However, some brown colour characteristics also resemble those described from subunit 1/4. In addition, AO25-7PC displays a gradual shift towards more olive-green colours near the base of the core.

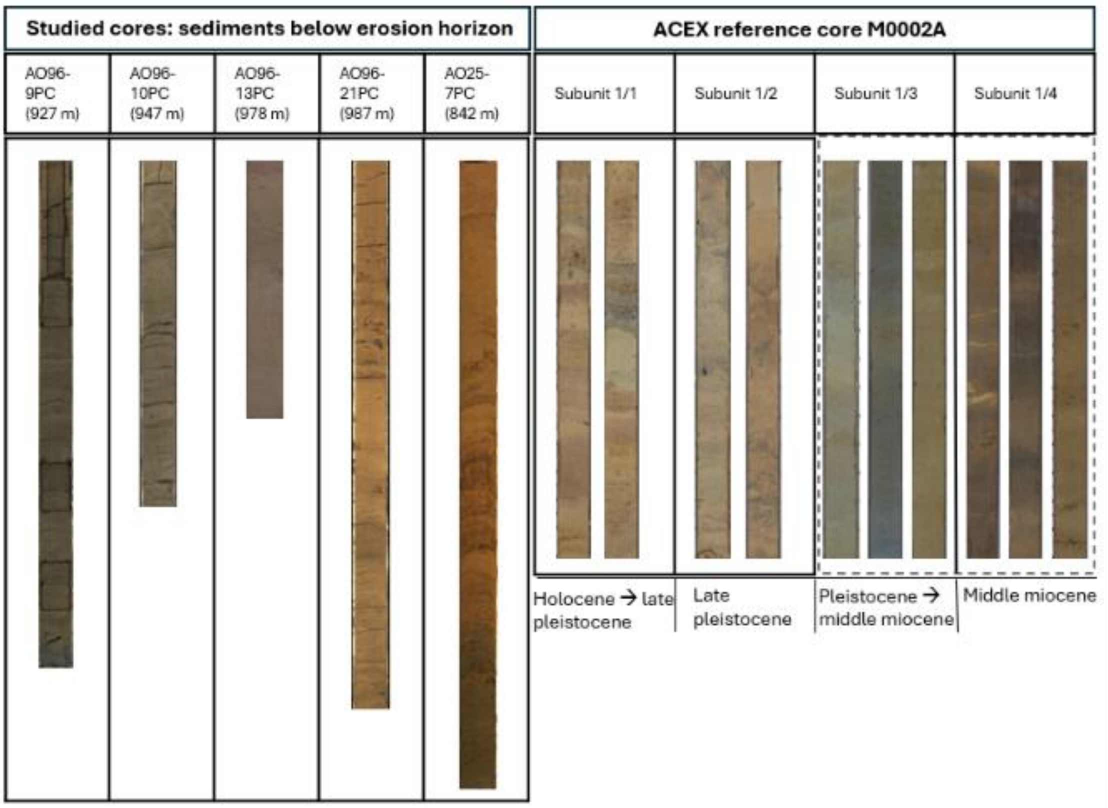

Figure 13. Comparison between sediments located beneath the interpreted erosion horizons in the studied cores and lithological subunits 1/1–1/4 of the ACEX reference core M0002A (IODP Expedition 302). The dashed outline highlights subunits 1/3 and 1/4, which display the strongest visual similarities to the studied sediments.

Stress history and erosion estimates

Estimations of the amount of eroded material at the sites are highly dependent on the selected *a* and *b* parameters. When applying the SHANSEP equation with parameters of a = 0.2 and b = 0.7, σv′ values range from 13.1 to 23.4 kPa, and OCR values range from 7.0 to 151.6. These correspond to σpc′ values between 146 and 1989 kPa, and translate into estimated eroded sediment thicknesses of 16 to 256 m (Table 2). It is unlikely that 256 meters were eroded from AO96-9PC, as sediments from an equivalent depth at ACEX are Paleogene organic and biosiliseous rich sediments.

Using parameters of a = 0.3 and b = 0.9, σv′ values remain the same, while OCR values range from 2.9 to 31.7. Corresponding σpc′ values range between 61 and 415 kPa, with estimated eroded sediment thicknesses between 5 and 52 m (Table 3).

Core	S_u (kPa)	Horizon depth (m)	Mean BD (g/cm^{-3})	*a*	*b*	σv′ (kPa)	OCR	σpc′ (kPa)	Eroded thickness (m)
AO96-9PC	88.21	1.70	1.806	0.2	0.7	13.1	151.6	1989	256
AO96-10PC	56.01	2.35	1.771	0.2	0.7	17.3	53.3	924	123
AO96-13PC	16.33	2.60	1.835	0.2	0.7	20.8	7.0	146	16
AO96-21PC	19.48	2.90	1.843	0.2	0.7	23.4	7.7	180	20
AO25-7PC	57.54	2.69	1.686	0.2	0.7	17.6	54.2	953	143

Table 2. SHANSEP-based calculations of effective vertical stress (σv′), overconsolidation ratio (OCR), preconsolidation stress (σpc′) and estimated eroded sediment thickness using parameters a = 0.2 and b = 0.7.

Core	S_u (kPa)	Horizon depth (m)	Mean BD (g/cm^{-3})	*a*	*b*	σv′ (kPa)	OCR	σpc′ (kPa)	Eroded thickness(m)
AO96-9PC	88.21	1.70	1.806	0.3	0.9	13.1	31.7	415	52
AO96-10PC	56.01	2.35	1.771	0.3	0.9	17.3	14.0	243	31
AO96-13PC	16.33	2.60	1.835	0.3	0.9	20.8	2.9	61	5
AO96-21PC	19.48	2.90	1.843	0.3	0.9	23.4	3.1	73	6
AO25-7PC	57.54	2.69	1.686	0.3	0.9	17.6	14.2	250	36

Table 3. SHANSEP-based calculations of effective vertical stress (σv′), overconsolidation ratio (OCR), preconsolidation stress (σpc′) and estimated eroded sediment thickness using parameters a = 0.3 and b = 0.9.

However, both approaches are consistent with the observation that lower shear strengths are found (and hence less eroded material predicted) from the deeper lying sites on the Lomonosov Ridge (Fig. 14). These differences in water depth are illustrated in the bathymetric profile across the sites (Fig. 15).

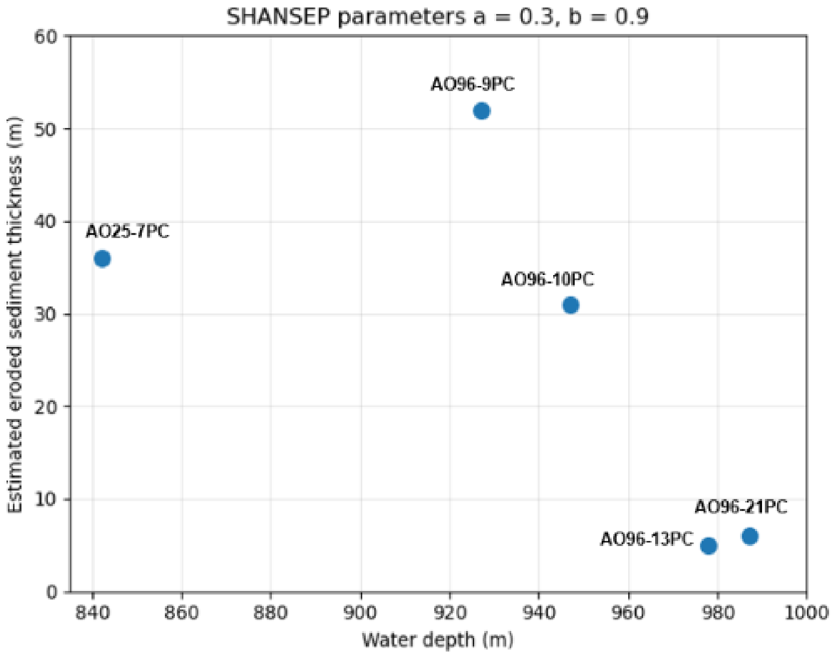

Figure 14. Estimated eroded sediment thickness plotted against water depth for the studied core sites using SHANSEP parameters a = 0.3 and b = 0.9.

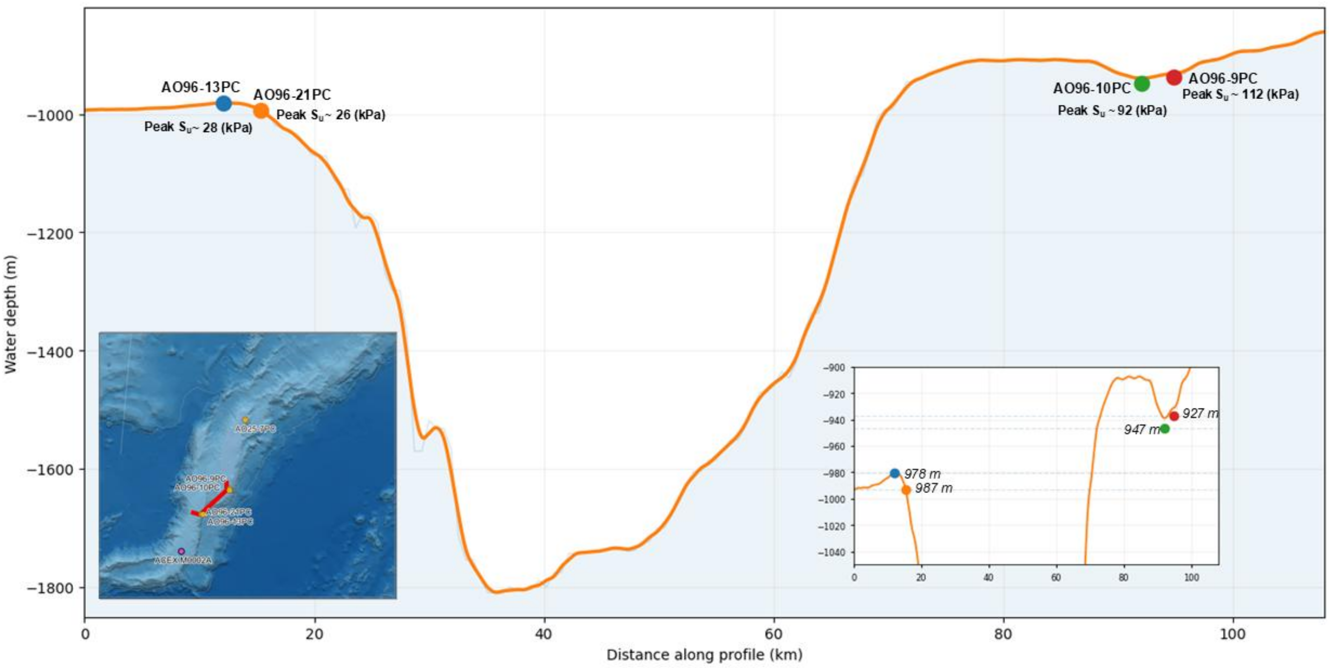

Figure 15. Bathymetric cross-section across the central segment of the Lomonosov Ridge showing the locations of sediment cores AO96-9PC, AO96-10PC, AO96-13PC and AO96-21PC. The inset map shows the location of the profile transect (red line).

Discussion

The OCR values ranging between 2.9 and 151.6 depending on the applied SHANSEP parameters indicate moderately to highly overconsolidated sediments below the erosion horizon implying that the overburden stress was greater in the past (Latoui & Rotta Loria, 2020). However, when assessing a sediment's OCR value, a number of factors need to be considered, including how time and loading together might have affected the sample, whether erosion during glacial impact has occurred, and the dynamics of pore water movement (O'Regan et al., 2010).

To further explore this, a calculation was performed to estimate the effective stress that would result if a floating ice shelf grounded on the Lomonosov Ridge. If the ice at the deeper sites only just scraped the seafloor at an approximate water depth of 980 m, then >45 m of ice not compensated by buoyancy would have grounded at the shallower sites. With an ice density of 915.1 kg m^{-3} (Yi & Zwally, 2009) this would equate to an applied effective stress of;

$$\sigma v' = \mathbf{z} * \rho i * g = 45 \text{ m} * 915.1 \text{ kg m}^{-3} * 9.82 \text{ m s}^{-2} = 404 \text{ kPa}$$

where;

ρi= ice density (kg m^{-3})
g= gravitational acceleration (9.82 m s^{-2})

This calculation results in a vertical applied stress of approximately 400 kPa, which is in the same range of the calculated ($\sigma pc'$) values derived using the higher assumed a and b constants (a = 0.3 and b = 0.9) in the SHANSEP equation (Table 3). This would suggest that grounding of a large floating ice shelf could potentially have generated stresses comparable to the OCR-based calculations.

However, geophysical evidence clearly documents the scouring and erosion of sediments which could also explain the higher overburden pressures in the past (the overconsolidated state of the sediments today). Previous sub-bottom data from the Lomonosov Ridge display evidence of large-scale glacial erosion in this region (Jakobsson et al., 2016). Based on truncated reflectors observed in high-resolution chirp sonar data, more than 50 m of sediment was estimated to have been removed at approximately 87°N on the ridge (O'Regan et al., 2010). The erosion estimates in this study indicate an interval ranging from 5 to 52 m (using a = 0.3 and b = 0.9), showing a similarity to these previous erosion estimates. The variations in OCR may be linked to the amount of sediment that was eroded. AO96-9PC and AO96-10PC are located at water depths 40–60 m shallower than AO96-13PC and AO96-21PC (Fig. 14). Although the sub-ice topography was likely quite varied, if we assume that the same general thickness of ice scoured both regions, then more material would be expected to be eroded from the shallower areas compared to the deeper ones.

To investigate this, a visual comparison was made between the sediments beneath the ice scouring horizon with the lithologic units described in the Neogene ACEX record (Fig. 13). If erosion varied substantially between the sites, one could argue that the shallower cores (AO96-9PC and AO96-10PC) would be expected to display more pronounced similarities to older ACEX strata than the deeper sites. The sediments beneath the erosion horizons show the strongest colour similarities with subunit 1/3 (17.38–168.53 mbsf in the ACEX record), although some brown colour characteristics also resemble subunit 1/4 (168.53–192.94 mbsf in the ACEX record).

Based on the estimated eroded sediment thicknesses, direct exposure of subunit 1/4-equivalent sediments appears unlikely. Since subunits 1/1 and 1/2 together comprise approximately 17 m of sediment in ACEX, erosion of approximately 5–50 m would be expected to expose sediments equivalent to subunit 1/2 or the upper part of subunit 1/3 rather than the much deeper subunit 1/4. Despite these observations, the comparison does not provide clear evidence that the shallower cores display stronger similarities to older ACEX strata than the deeper cores. Instead, the sediments beneath the erosion horizons show mixed lithological characteristics and colour variations, making it difficult to confidently link individual cores to specific ACEX subunits or ages based on visual comparison alone.

The acoustically transparent unit (AU2) has previously been interpreted as remoulded sediment, where deformation has destroyed the original stratification and removed coherent acoustic reflectors. Deformation and remoulding are common in mass transport deposits and are readily seen through visual description and are sometimes even more pronounced in CT images. An example of this comes from AO16-11-PC1 which contains a mass transport deposit, with very pronounced indications of ductile deformation and remoulding (Fig. 16). It was anticipated that a similar level of deformation would be seen in some of the cores from beneath the glacial erosion horizon if the sediments were completely remoulded as suggested by O'Regan et al., (2010). However, the AO96 cores and AO25-7PC display only subtle signs of deformation in the CT images raising questions regarding this interpretation and highlighting the complexity of linking acoustic transparency directly to sediment deformation.

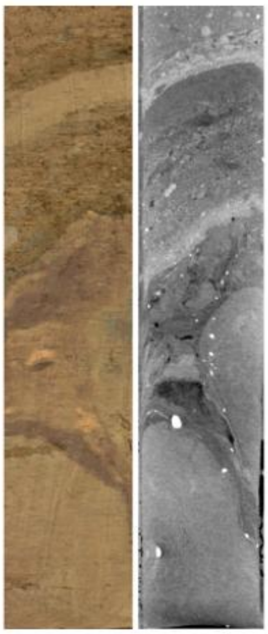

Figure 16. Core photograph and corresponding CT image of the reference core AO16-11-PC1 showing pronounced soft-sediment deformation and remoulding within a mass transport deposit. This reference core is included to illustrate the scale and appearance of deformation structures that may develop in unconsolidated sediments. In comparison, only subtle indications of deformation are observed in the AO96 cores and AO25-7PC.

Generally, only subtle sub-horizontal features, that may represent shear bands (Taira et al., 1992), can be observed in AO96-9PC, AO96-10PC and AO96-13PC. Furthermore, none of the studied cores display the completely homogenised appearance that might be expected if extensive high-strain deformation had affected the sediments (Hart and Boulton, 1991). The fact that these sediments also lack evidence of faulting may also indicate that strain and deformation were limited in extent (Cornejo et al., 2025).

Existing evidence, including the limited occurrence of extensive deformation structures in CT images, OCR-based estimates indicating different loading and erosion histories, and the consistent geotechnical patterns observed across all five studied cores, supports the interpretation that the geotechnical properties of the sediments beneath the glacial erosional surface are largely inherited from the amount of material that was eroded, and not the degree of deformation. However, further work is needed to confirm this.

When applying the SHANSEP equation, the parameters *a* and *b* should be empirically determined from laboratory observations and differ between soil types (Larsson, 1980). When using the different combinations of *a* and *b*, substantial differences in the calculated values were observed, affecting OCR and estimated eroded sediment. Future work should aim to establish the magnitude and variability of these parameters for central Arctic Ocean sediments.

Additional uncertainties regarding the calculations that should be considered are that the eroded sediment load was represented using mean bulk density values above the erosion horizon, which may overlook variations in sediment properties downcore. Another aspect is that average Su values were calculated from individually selected intervals below the erosion horizon, and different interval selections may therefore influence the calculated values. Small, but possible uncertainties in the interpreted erosion horizon depth may also affect the calculations.

The lack of notable deformation structures in the CT data does not automatically rule out internal deformation. Although the CT images were acquired at a relatively high resolution (voxel size = 125 µm), limitations related to image resolution and the detectability of subtle sediment structures should still be considered. In a study where a 0.3 mm resolution was used, the authors emphasized the effectiveness of CT scanning for identifying internal structures and sedimentary facies, while also noting that resolution limitations may affect the detectability of smaller-scale features (Emmanouilidis et al., 2020). Furthermore, evidence of subglacial deformation is commonly identified using microstructural observations on thin sections, where grain fabrics, grain rotation and small-scale deformation structures can be observed (van der Meer, 1993). This would be a worthwhile follow-up study to this work to more firmly assess the degree of deformation in the underlying sediments.

Conclusions

Large-scale glacial erosion of the central Lomonosov Ridge is clearly evidenced by geophysical data. Sediment cores that penetrate the erosional horizon display varied geotechnical properties, notably in their undrained shear strength. Past work has suggested that these differences arise from variable degrees of subglacial remoulding, a process inferred from interpretation of sub-bottom data, and a process well-described by classical studies on subglacial tills. However, CT-scanning failed to identify notable signs of deformation, suggesting that the geotechnical properties beneath the erosion horizon may primarily reflect the amount of sediment that has been eroded, rather than the degree of deformation or remoulding.

The results presented in this study contribute to the existing knowledge of the central segment of the Lomonosov Ridge and the processes of subglacial deformation. The results provide a basis for future investigations into the interpretation of geophysical data and sediment physical properties in areas of glacial scouring.

References

Kristoffersen, Y., Hall, J.K. & Harris Nilsen, E. The Lomonosov Ridge, central Arctic Ocean – the world's longest submarine ridge of continental origin: outline of the history of exploration, morphology, sediment deposition and exhumation of the North American and Central ridge segments. *Journal of the Geological Society.* Volume: 182 (2024). https://www.lyellcollection.org/doi/full/10.1144/jgs2024-095

Jokat, W., Uenzelmann-Neben, G., Kristoffersen, Y. & Rasmussen, T.M. *Lomonosov Ridge—A double-sided continental margin*. *Geology*. 20:10 (1992): p. 887–890. https://www.researchgate.net/publication/249519728_Lomonosov_Ridge---A_double-sided_continental_margin

Jakobsson, M. First high-resolution chirp sonar profiles from the central Arctic Ocean reveal erosion of Lomonosov Ridge sediments. *Marine Geology.* Volume: 152: 1-4 (1999): p.111-123. https://doi.org/10.1016/S0025-3227(98)00186-8

Crane, K., Vogt, P.R. & Sundvor, E. Deep Pleistocene Iceberg Plowmarks on the Yermak Plateau. *Glaciated Continental Margins: An Atlas of Acoustic Images*. London: Chapman & Hall (1997): p. 140–141. https://link.springer.com/chapter/10.1007/978-94-011-5820-6_54

Polyak, L., Edwards, M.H., Coakley, B.J. & Jakobsson, M. Ice shelves in the Pleistocene Arctic Ocean inferred from glaciogenic deep-sea bedforms. *Nature*. Volume: 410(6827): p.427-428 & p.453–457 (2001). https://www.researchgate.net/publication/12071480_Ice_shelves_in_the_Pleistocene_Arctic_Ocean_inferred_from_deep-sea_bedforms

Jakobsson, M., Nilsson, J., Andersson, L., Backman, J., Björk, G., Cronin, T.M., Kirchner, N., Koshurnikov, A., Mayer, L., Noormets, R., O'Regan, M., Stranne, C., Ananiev, R., Barrientos Macho, N., Cherniykh, D., Coxall, H., Eriksson, B., Flodén, T., Gemery, L., Gustafsson, Ö., Jerram, K., Johansson, C., Khortov, A., Mohammad, R. & Semiletov, I. Evidence for an ice shelf covering the central Arctic Ocean during the penultimate glaciation. *Nature communications.* Volume: 7: 10365 (2016). https://doi.org/10.1038/ncomms10365

O'Regan, M., Jakobsson, M. & Kirchner, N. Glacial geological implications of overconsolidated sediments on the Lomonosov Ridge and Yermak Plateau. *Quaternary Science Reviews*. Volume: 29: 25-26 (2010): 3532-3544. https://www.sciencedirect.com/science/article/pii/S0277379110003318

Cornejo, C., Campos, C. & Guzmán, O. Soft-sediment deformation structures induced by seismic activity in the Upper Cretaceous Tena Formation - Oriente basin of Ecuador. *Journal of South American Earth Sciences*. Volume: 153 (2025): 105365. https://doi.org/10.1016/j.jsames.2025.105365

Stow, D.A.V. & Aksu, A.E. Disturbances in soft sediments due to piston coring. *Marine Geology*. Volume: 28: 1-2 (1978): 135-144. https://doi.org/10.1016/0025-3227(78)90101-9

Hart, J.K. & Boulton, G.S. The interrelation of glaciotectonic and glaciodepositional processes within the glacial environment. *Quaternary Science Reviews*. Volume: 10: p. 335–350 (1991). https://www.sciencedirect.com/science/article/pii/027737919190035S

van der Meer, J.P.M. Microscopic evidence of subglacial deformation. *Quaternary Science Reviews*. Volume: 12: 7 (1993): p. 553-587. https://www.sciencedirect.com/science/article/pii/027737919390069X

Clarke, G.K.C. Subglacial Processes. *Annual Review of Earth and Planetary Sciences*. Volume: 33: 247-276 (2005). https://www.researchgate.net/publication/51992184_Subglacial_Processes

Narloch, W., Phillips, E.R., Piotrowski, J.A. & Ćwiek, M. Patterns of deformation within a subglacial shear zone: Implications for palaeo-ice stream bed evolution. *Sedimentary Geology*. Volume: 397: 105569. (2020). https://www.sciencedirect.com/science/article/pii/S0037073819302210

Robinson, D.E., Menzies, J., Wellner, J.S. & Clark, R.W. Subglacial sediment deformation in the Ross Sea, Antarctica. *Quaternary Science Advances*. 4: 100029 (2021). https://doi.org/10.1016/j.qsa.2021.100029

Kassou, F., Ben Bouziyane, J., Ghafiri, A. & Sabihi, A. Slope Stability of Embankments on Soft Soil Improved with Vertical Drains. *Civil Engineering Journal*. Volume: 6(1) (2020): 164–173. https://www.researchgate.net/publication/338545807_Slope_Stability_of_Embankments_on_Soft_Soil_Improved_with_Vertical_Drains

Expedition 302 Scientists. Expedition 302 Summary. *Proceedings of the Integrated Ocean Drilling Program*. Volume: 302 (2006). doi:10.2204/iodp.proc.302.106.2006

Latoui, L. & Rotta Loria, A.F. Chapter 5 - Thermohydromechanical behaviour of soils and soil–structure interfaces. *Analysis and Design of Energy Geostructures*. (2020): p. 209-269. https://doi.org/10.1016/B978-0-12-816223-1.00005-9

Robinson, D.A., Friedman, S.P., Thomas, A., Hirmas, D., Sullivan, P.L. & Nemes, A. Soil bulk density and porosity connecting macro- and micro-scales through geometry. *Earth-Science Reviews*. Volume: 268: 105173 (2025). https://doi.org/10.1016/j.earscirev.2025.105173

Taira, A., Hill, I., Firth, J., Berner, U., Brückmann, W., Byrne, T., Chabernaud, T., Fisher, A., Foucher, J.-P., Gamo, T., Gieskes, J., Hyndman, R., Karig, D., Kastner, M., Kato, Y., Lallement, S., Lu, R., Maltman, A., Moore, G., Moran, K., Olafsson, G., Owens, W., Pickering, K., Siena, F., Taylor, E., Underwood, M., Wilkinson, C., Yamano, M. & Zhang, J. Sediment deformation and hydrogeology of the Nankai Trough accretionary prism: Synthesis of shipboard results of ODP Leg 131. *Earth and Planetary Science Letters*. Volume: 109 (1992): p. 431–450. https://www-odp.tamu.edu/publications/131_SR/VOLUME/CHAPTERS/sr131_reprint04.pdf

Li, Y., Luo, T., Sun, X., Liu, W., Li, Q., Li, Y. & Song, Y. Strength Behaviors of Remolded Hydrate-Bearing Marine Sediments in Different Drilling Depths of the South China Sea. *Energies*. Volume: 12: 2 (2019): 253. https://doi.org/10.3390/en12020253

Song, S. & Cao, Y. Textures and Structures of Metamorphic Rocks. *Encyclopedia of Geology (Second Edition)*. (2021): p. 375-388. https://doi.org/10.1016/B978-0-08-102908-4.00052-7

Larsson, R. Undrained shear strength in stability calculation of embankments and foundations on soft clays. *Canadian Geotechnical Journal*. Volume: 17 (1980): 591-602. https://www.scribd.com/document/379171520/Larsson-1980

Emmanouilidis, A., Messaris, G., Ntzanis, E., Zampakis, P., Prevedouros, I., Bassukas, D.A. & Avramidis, P. CT scanning, X-ray fluorescence: Non-destructive techniques for the identification of sedimentary facies and structures. *Revue de Micropaléontologie*. Volume: 67: 100410 (2020). https://doi.org/10.1016/j.revmic.2020.100410

Yi, D. & Zwally, H.J. *Arctic Sea Ice Freeboard and Thickness*, *Version 1*. Boulder, Colorado USA. NASA National Snow and Ice Data Center Distributed Active Archive Center. (2009, updated 2014). https://nsidc.org/sites/default/files/nsidc-0393-v001-userguide_1.pdf [accessed: 2026-06-08]

Appendix A

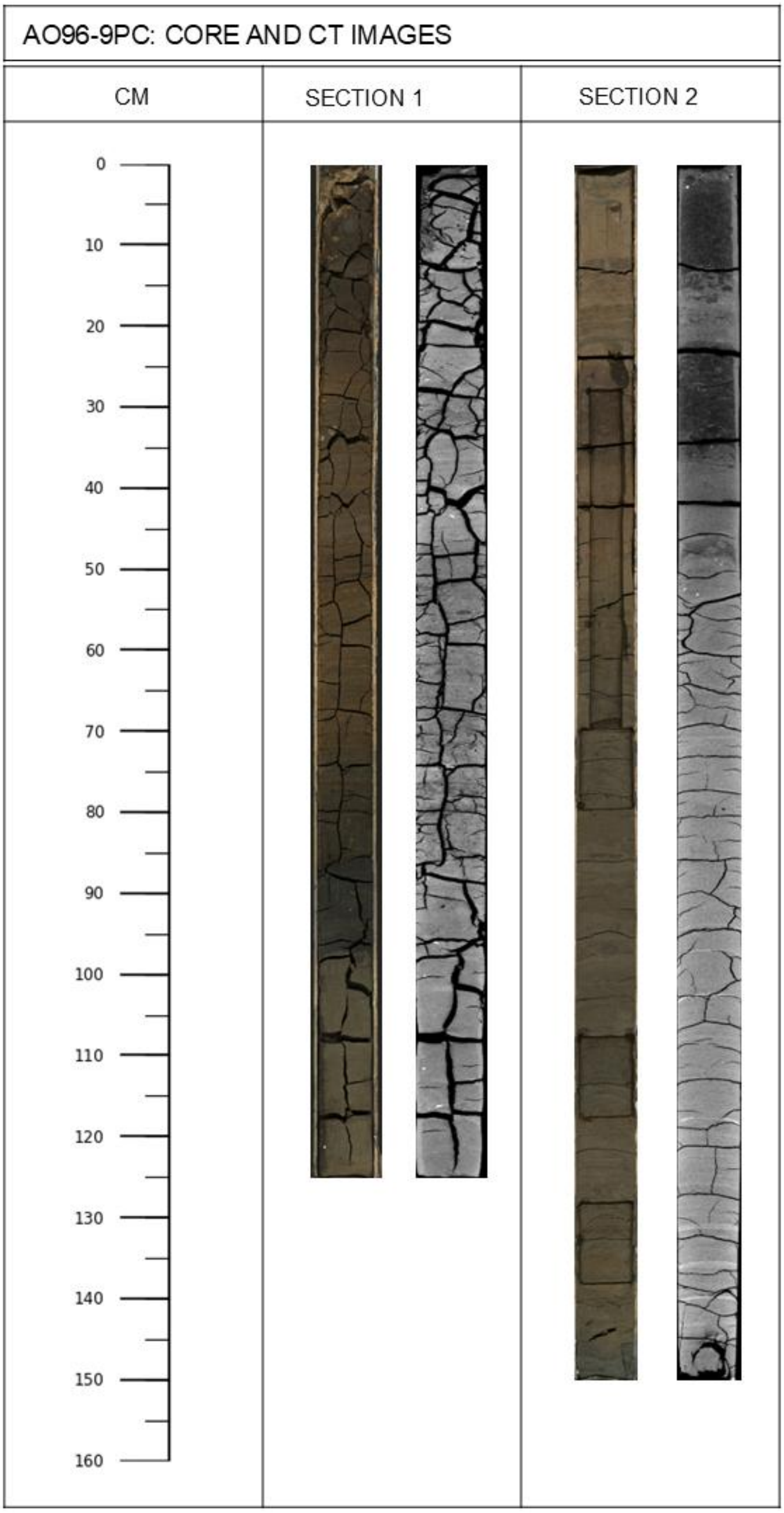

Figure A1. Complete core photo table of AO96-9PC, including core photograph and corresponding CT image.

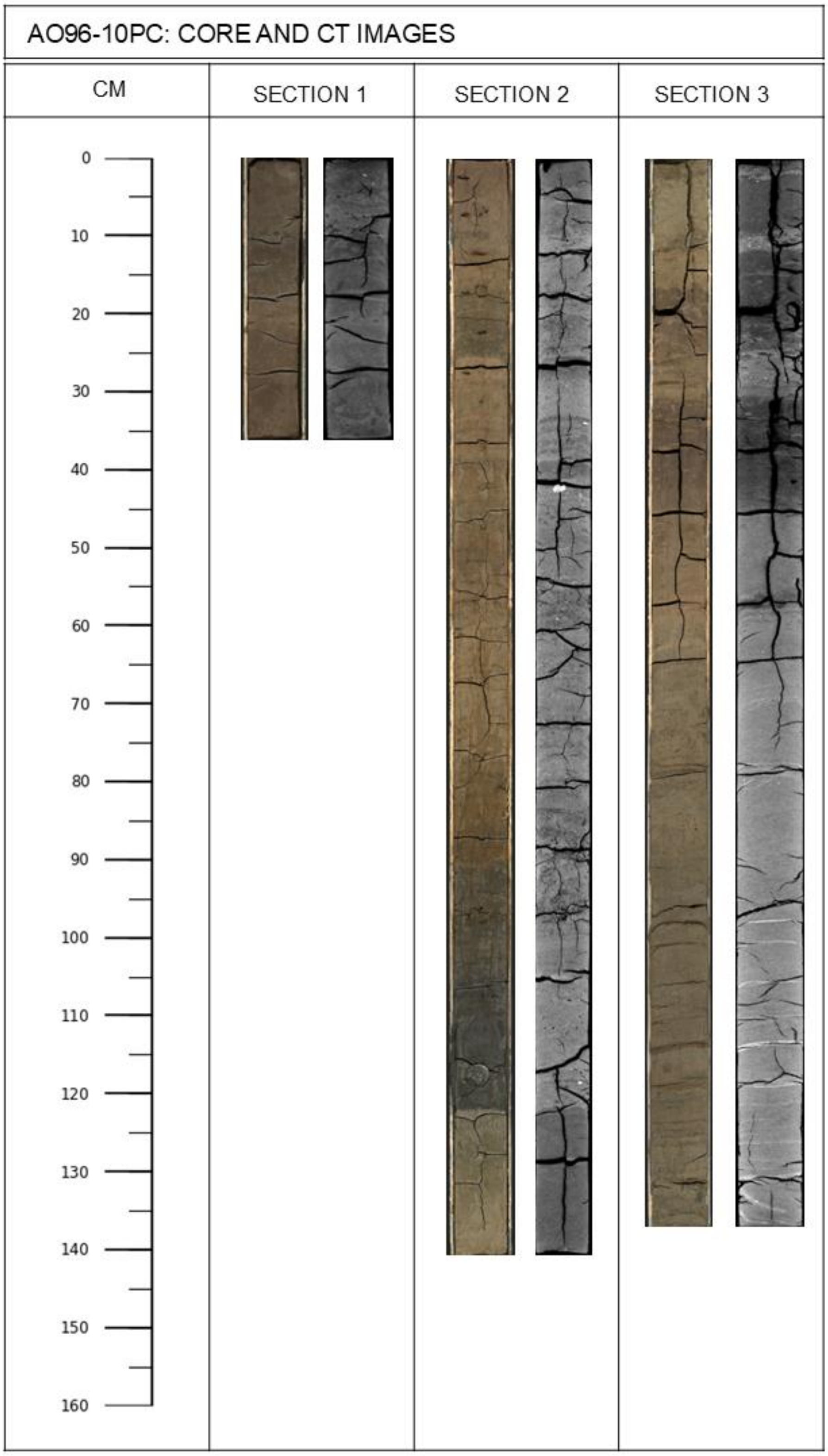

Figure A2. Complete core photo table of AO96-10PC, including core photograph and corresponding CT image.

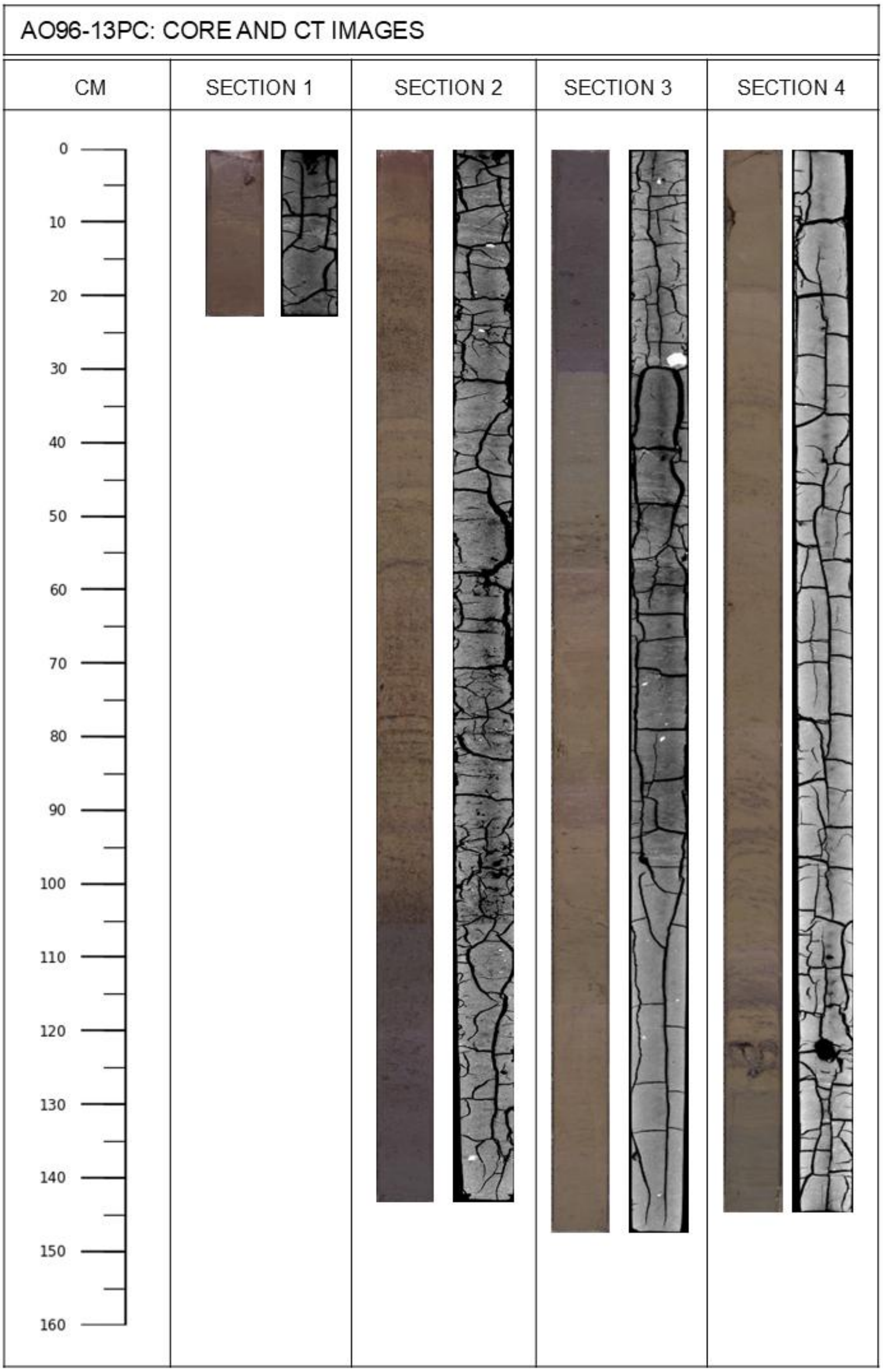

Figure A3. Complete core photo table of AO96-13PC, including core photograph and corresponding CT image.

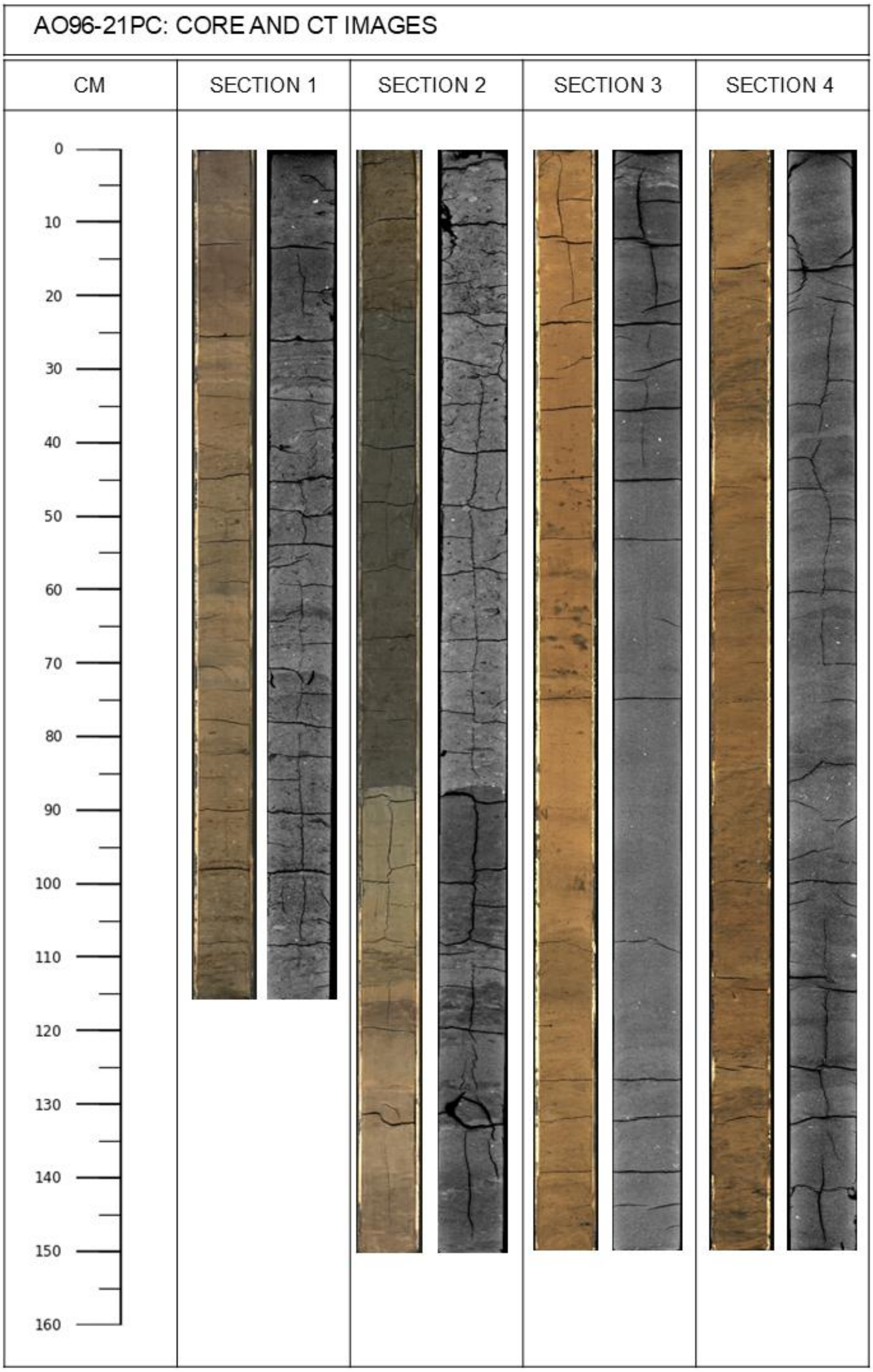

Figure A4. Complete core photo table of AO96-21PC, including core photograph and corresponding CT image.

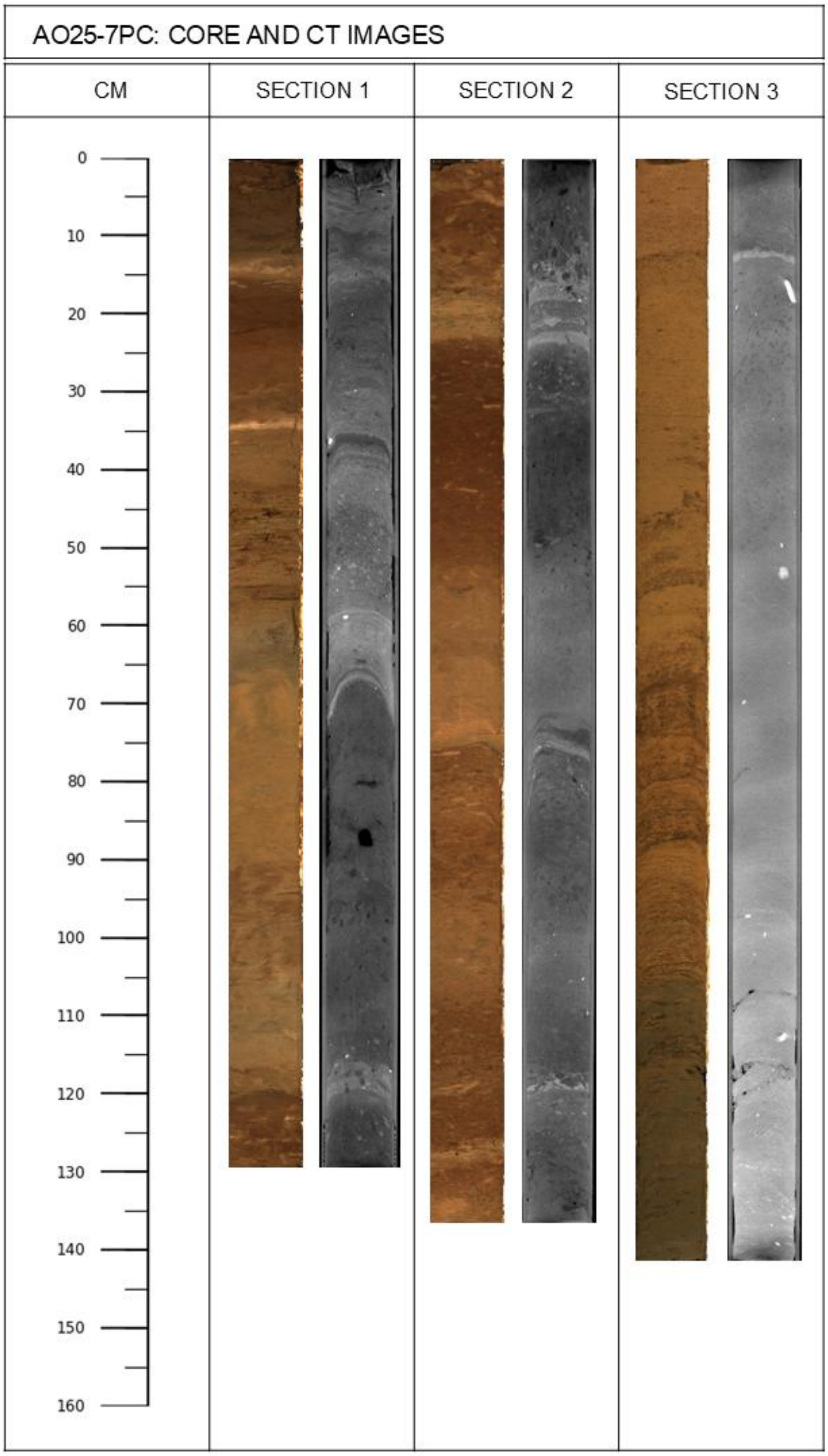

Figure A5. Complete core photo table of AO25-7PC, including core photograph and corresponding CT image.

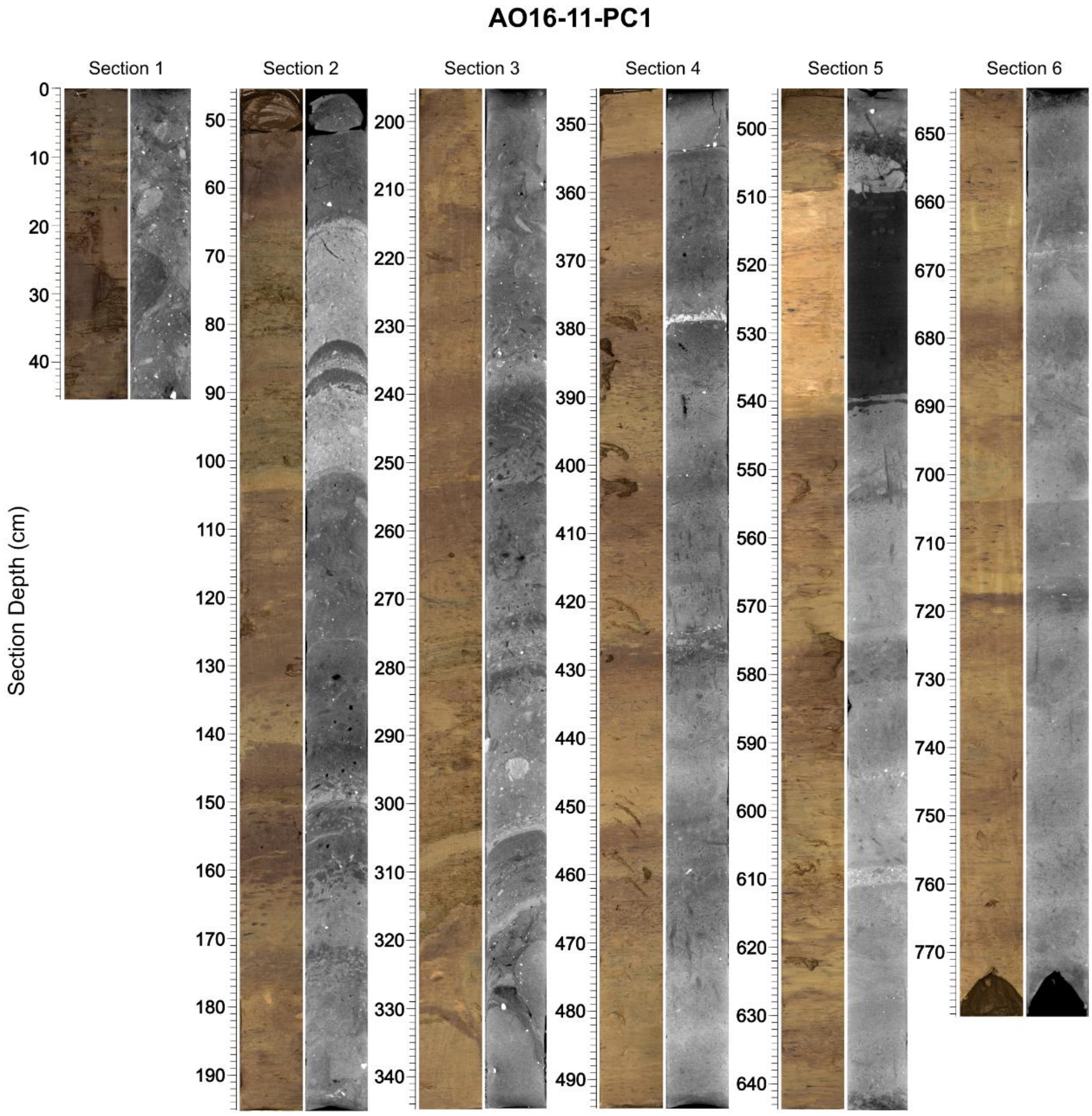

Figure A6. Complete core photo table of the reference core AO16-11-PC1, including core photographs and corresponding CT images. The core contains a mass transport deposit with pronounced soft-sediment deformation and remoulding and is included as a reference for comparison with the studied Lomonosov Ridge cores.